DEVELOPMENTAL BIOLOGY

A dominant tubulin mutation causes cerebellar neurodegeneration in a genetic model of tubulinopathy

Sofia Fertuzinhos[1]†, Emilie Legué[1]†, Davis Li[2], Karel F. Liem Jr.[1]*

Mutations in tubulins cause distinct neurodevelopmental and degenerative diseases termed "tubulinopathies"; however, little is known about the functional requirements of tubulins or how mutations cause cell-specific pathologies. Here, we identify a mutation in the gene *Tubb4a* that causes degeneration of cerebellar granule neurons and myelination defects. We show that the neural phenotypes result from a cell type–specific enrichment of a dominant mutant form of *Tubb4a* relative to the expression other β-tubulin isotypes. Loss of *Tubb4a* function does not underlie cellular pathology but is compensated by the transcriptional up-regulation of related tubulin genes in a cell type–specific manner. This work establishes that the expression of a primary tubulin mutation in mature neurons is sufficient to promote cell-autonomous cell death, consistent with a causative association of microtubule dysfunction with neurodegenerative diseases. These studies provide evidence that mutations in tubulins cause specific phenotypes based on expression ratios of tubulin isotype genes.

INTRODUCTION

Microtubules (MTs) are fundamental cytoskeletal components present in all eukaryotic cells. They are involved in multiple essential functions in neuronal development such as cell division, cell motility, cell scaffolding, and axonal transport (*1*). MTs are composed of heterodimers of α- and β-tubulin proteins. At least eight α-tubulin and eight β-tubulin isotypes exist in mammals, each encoded by separate, highly conserved genes. Patient sequencing studies have identified mutations in the various tubulin isotype genes that cause a large number of developmental and degenerative disorders, termed "tubulinopathies" (*2*). Although MTs are ubiquitous structures, mutations in individual tubulin genes cause notably specific disease phenotypes, most commonly in the central nervous system (CNS). These include developmental defects of the cerebral cortex such as lissencephaly, polymicrogyria, pachygyria (*TUBB2A*, *TUBA1A*, *TUBB3*, and *TUBB2B*), and microcephaly (*TUBB5*) (*3–11*). Other neuronal phenotypes associated with mutations in tubulin isotype genes include ocular motility disorders (*TUBB3*) (*12*, *13*), retinal degeneration and hearing loss (*TUBB4B*) (*14*), and familial and sporadic cases of amyotrophic lateral sclerosis (*TUBA4A*) (*15*, *16*). Nonneural diseases caused by tubulin mutations include thrombocytopenia (*TUBB1*) (*17*) and infertility (*TUBB8*) (*18*). Recently, mutations in the β-tubulin gene *TUBB4A* has been identified in patients with a spectrum of neurological disorders including H-ABC leukodystrophy [hypomyelination with atrophy of the basal ganglia and cerebellum; Online Mendelian Inheritance of Man (OMIM) 612438] (*19–21*), primary dystonia [dystonia 4 (DYT4) dystonia/whispering dysphonia; OMIM 128101] (*22*, *23*), and isolated cases of hypomyelination (*24*). While MTs are essential for many basic cellular processes, the mechanisms by which mutations in individual tubulin genes result in distinct disease phenotypes are not understood.

The tubulin isotype proteins are highly homologous and differ mainly in their C-terminal amino acid sequences, the site where numerous posttranslational modifications influence MT interactions (*25–27*). The distinct tubulin isotype genes are highly conserved evolutionarily, suggesting that they have functional significance (*28*). In *Drosophila*, substitutions of tubulin isotypes in vivo were found to result in MT defects, indicating that the tubulin isotype genes are not functionally equivalent with respect to MT functionality (*29*). In vitro and in vivo studies have shown that MT stability and MT protofilament number are regulated in part by β-tubulin isotype composition (*30*, *31*). While MTs are ubiquitous and tubulin genes are broadly expressed, β-tubulin isotype genes have also been shown to have temporal and cell-specific expression patterns during mammalian development including the nervous system (*32*, *33*). These findings along with the distinct organ pathologies seen in patients with tubulinopathy are consistent with the idea of a "tubulin code" that postulates that the tubulin isotype composition of MT influences its properties, in part through regulating posttranslational modifications (*34*, *35*), which in turn could be used by the cells for specific processes in a "multitubulin hypothesis" (*36*). Analysis of mouse lines harboring tubulin isotype gene mutations has been useful to model human disease phenotypes and to test the requirement of tubulin isotype genes (*2*). Knockout alleles of *Tubb5* (*37*) and *Tubb1* (*17*) show that these tubulin isotypes are essential for mouse development with the loss-of-function phenotypes resembling the human pathologies. However, deletion of other tubulin isotype genes in mice shows only minor defects that do not recapitulate the human disease phenotypes (*38*, *39*), indicating that certain tubulin isotype genes are functionally redundant in mice. Nearly all patient disease mutations identified in tubulin genes are de novo missense mutations. However, it has yet to be established whether the distinct disease phenotypes in tubulinopathies are due to the differential requirements of tubulin isotype genes in the various tissues affected. It is also unclear whether the dominant phenotypes are caused by a haploinsufficiency or dominant negative activity (*40*).

Here, we identify a dominant mutation in the tubulin isotype gene *Tubulin beta 4a* (*Tubb4a*) from a forward genetic screen in the mouse. Mice harboring the *Jittering* mutation develop notable degenerative phenotypes affecting cerebellar granule cell neurons (GCNs) and myelination, which parallels patients with a severe encephalopathic variant form of the rare neurological disorder

[1]Vertebrate Developmental Biology Program, Department of Pediatrics, Yale University School of Medicine, New Haven, CT 06520, USA. [2]Department of Genetics, Yale University School of Medicine, New Haven, CT 06520, USA.
*Corresponding author. Email: karel.liem@yale.edu
†These authors contributed equally to this work.

H-ABC (*21*). Through the generation and analysis of a *Tubb4a* allelic series in the mouse, which combines a missense mutation with a targeted null allele, we propose a model for the genetic basis of CNS pathology in the mutant mice that depends on the expression ratio of the mutant tubulin in relation with other β-tubulin family members and not on *Tubb4a* loss of function. Our studies show that a dominant tubulin mutation is sufficient to cause the death of differentiated neurons in vivo in a cell-autonomous and dosage-dependent manner. This work sheds light on the genetic mechanisms of cell-specific pathologies in tubulinopathies.

RESULTS

### A missense mutation in *Tubb4a* causes myelination and cerebellar defects

To identify genes required for nervous system development, in the mouse, we performed a three-generation *N*-ethyl-*N*-nitrosourea (ENU)-driven forward genetic screen (*41*). We isolated the mutant mouse line *Jittering* (*Jit*) that developed a tremulous phenotype commencing at postnatal day 10 (P10) (movie S1). Homozygous *Jit* mice were born at Mendelian ratios with mutants becoming increasingly ataxic and prone to tonic seizures. Homozygous *Jit* mice were analyzed on the FVB background and typically survived up to ~7 weeks. Gross inspection of the brain and spinal cord from mutant animals at P48 showed reduced cerebellar volume and diminished white matter tracts compared with wild-type (WT) littermates (Fig. 1, A to C). To define the molecular basis of the *Jit* phenotype, we performed meiotic recombination mapping to identify the causative mutation. The mutation mapped to a ~185-kb region on mouse chromosome 17 based on linkage to mutagenized B6 chromosomes using single-nucleotide polymorphism (SNP) and simple sequence length polymorphism (SSLP) markers. Among the genes within the interval was *Tubb4a*, a gene previously associated with neurological diseases in patients including myelination disorders, cerebellar pathologies, and primary dystonia. We sequenced *Tubb4a* from homozygous *Jit* mice and uncovered a T-to-A transition that resulted in an asparagine-to-lysine missense at position 414 (N414K) (fig. S1A). Asparagine 414 is conserved in tubulin proteins from yeast to human and resides in helix 12 (H12), a domain essential for kinesin interactions (fig. S1, B and C).

The diminished white matter tracks evident in whole brains and the association of *Tubb4a* with leukodystrophy in patients suggested defects in myelination. We therefore analyzed myelin by eriochrome (Eri-C) staining on coronal sections through the CNS of *Tubb4a*$^{Jit/Jit}$ mutants at P48, which showed a severe reduction of central myelin in all CNS regions including the forebrain and spinal cord compared with WT controls (Fig. 1, D to G and J). Eri-C staining was present in the motor and sensory nerves of *Tubb4a*$^{Jit/Jit}$ mutants, indicating that peripheral myelination was preserved (Fig. 1, F and G). CNS sections stained with Nissl revealed thinned white matter tracts evident in the corpus callosum (CC) and the spinal cord, consistent with reduced myelination (Fig. 1, H and I). Measurements of the CC thickness showed a significant decrease in the *Jit* CC thickness compared with WT (Fig. 1K). However other regions of the CNS appeared less affected, as the neocortex thickness and layer organization in *Jit* mutants and WT (Fig. 1, H, I, and L) were similar. These results showed severe deficits in myelination in *Jit* mice at P48. These results are consistent with previous reports showing hypomyelination phenotypes due to *Tubb4a* mutations in rodent models (*20*, *42*).

To test whether the hypomyelination observed in *Tubb4a*$^{Jit/Jit}$ mutant mice was due to myelin degeneration or a failure to develop myelin, we performed a histochemical analysis of myelination at P12, P21, and P48 by Eri-C staining. Myelination in the CNS normally commences at early postnatal ages in the mouse, progressing from posterior to anterior in the brain and increasing as mice mature to adulthood. In sagittal sections through the WT CNS, we found Eri-C staining in posterior regions including the brainstem and cerebellum at P12 (Fig. 1M) and increasing in intensity by P21 (Fig. 1O), and by P48, strong Eri-C staining was present throughout the CNS (Fig. 1Q). In contrast, we failed to detect clear Eri-C staining in *Tubb4a*$^{Jit/Jit}$ mutants at any age tested (Fig. 1, N, P, and R). In addition, at P48, the mutant cerebellum lacked myelin and appeared notably reduced in volume (Fig. 1R) compared with WT or mutants at earlier ages (Fig. 1, M to R). Oligodendrocytes (OLs) are the cells responsible for myelination in the CNS; they populate the white matter tracts where they myelinate and support axons. To determine whether the lack of myelination was due to OL cell death in *Jit* mutants, we performed immunohistochemistry with an antibody against cleaved caspase-3 (CASP3). We found numerous CASP3-positive cells populating the CC at P21 compared with WT controls (Fig. 1, S and T) and some CASP3-positive cells in the remnant CC at P48, while dying cells were virtually absent from WT CC, indicating progressive cell death of OLs in *Tubb4a*$^{Jit/Jit}$ mutant mice. To further characterize the paucity of myelin in the mutants, we performed transmission electron microscopy (TEM) on the CC of *Tubb4a*$^{Jit/Jit}$ mice. At both P21 and P48, *Tubb4a*$^{Jit/Jit}$ mutants showed severe deficits in myelination compared with WT littermates, with axons clearly present but mostly with absent myelin sheaths compared with WT controls (Fig. 1, U, V, Y, and Z). The TEM data were consistent with the Eri-C histological and CASP3 immunohistological analyses and showed OL cell death with a profound failure in the development of myelin in the CNS of *Tubb4a*$^{Jit/Jit}$ mutants.

### The *Jittering* mutation causes progressive degeneration of cerebellar GCNs

The temporal analysis of myelination in brain sagittal sections also showed a notable reduction in the size of the cerebellum at P48 (Fig. 1R) compared with WT or mutants at earlier ages (Fig. 1, M to R). Atrophy of the *Tubb4a*$^{Jit/Jit}$ mutant cerebellum (Cb) was more severe than could be accounted for by the lack of myelin, so we next examined Cb cytoarchitecture in *Tubb4a*$^{Jit/Jit}$ mutants over time. Nissl staining of sagittal sections of the Cb examined at P21 showed similar morphology in *Tubb4a*$^{Jit/Jit}$ and WT mice, except for the thinned white matter tracks resulting from lack of myelination (Fig. 2, A and B, and fig. S2, A and B). The stereotypical laminar organization of the Cb appeared similar in *Tubb4a*$^{Jit/Jit}$ and WT animals as well as the inner granule cell layer (IGL) surface area (Fig. 2, A to C). However, by P35, the size of the *Tubb4a*$^{Jit/Jit}$ Cb was reduced compared with WT, and the IGL and molecular layer (ML) in the *Tubb4a*$^{Jit/Jit}$ Cb were thinner than in the WT Cb (Fig. 2, D and E). The IGL surface area was significantly diminished in *Tubb4a*$^{Jit/Jit}$ mutants compared with WT, consistent with atrophy of this layer (Fig. 2F). By P48, the IGL was nearly absent with few granule cells present, and the ML thickness was further reduced in *Tubb4a*$^{Jit/Jit}$ mutants compared with WT (Fig. 2, G to I). The progressive IGL and ML thinning were consistent with a loss of GCNs, whose cell bodies populate the IGL and whose axons project to the ML. These data indicated that during development, GCN production was similar to WT, but GCNs
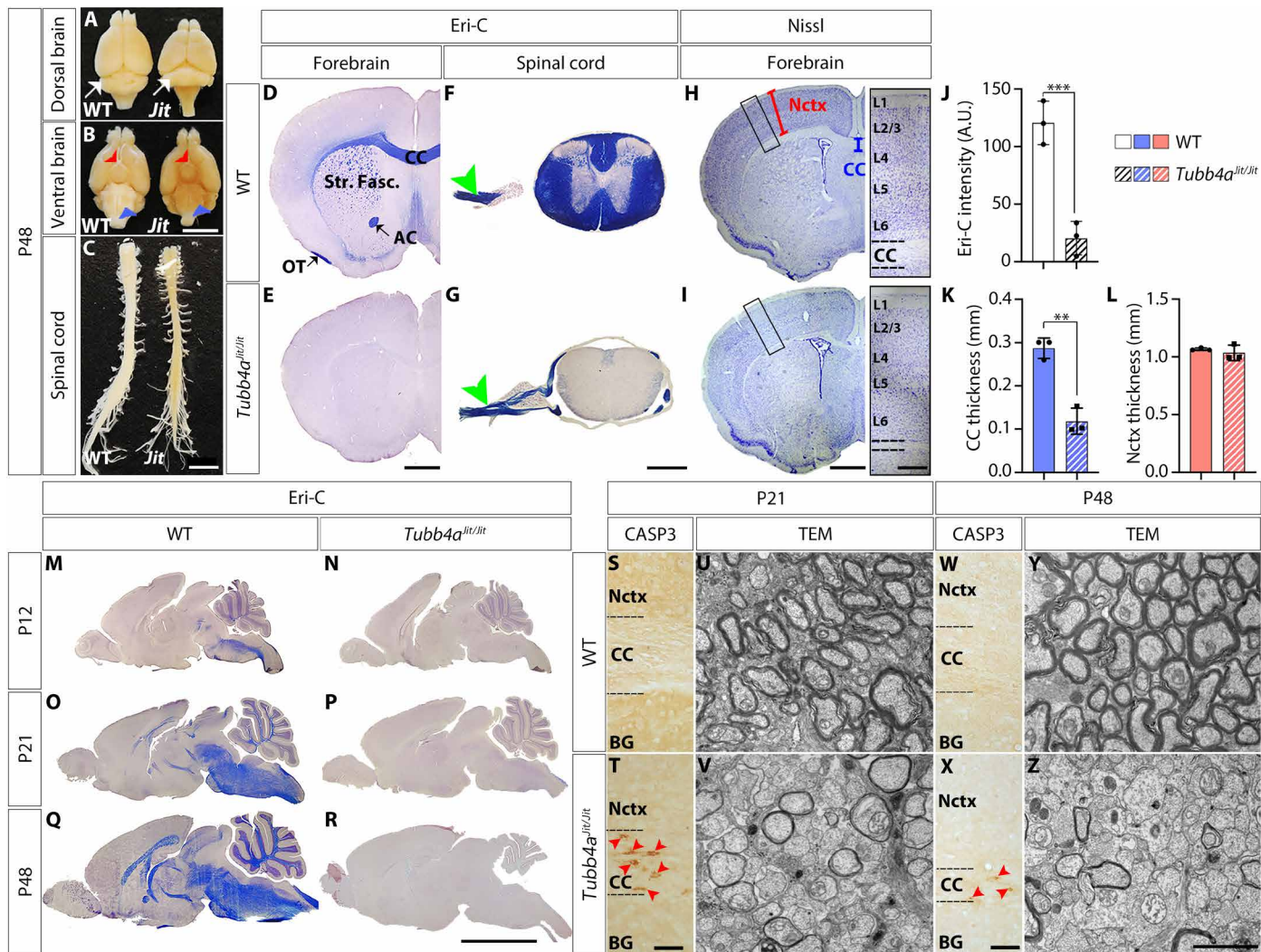
Fig. 1. *Jittering* (*Tubb4a^Jit/Jit*) mutants display CNS white matter defects. (**A** to **C**) P48 WT and *Jittering* CNS [dorsal (A), ventral (B) brain, and spinal cord (C)] showing reduction of cerebellum (white arrow) and white matter [brainstem (blue arrowheads) and optic chiasm (red arrowheads)] in *Jittering*. Scale bars, 5 mm. (**D** to **G**) Eri-C staining (blue) of forebrain (D and E) and spinal cord (F and G) coronal sections from WT and *Tubb4a^Jit/Jit* P48 animals. Scale bars, 1 mm (forebrain) and 500 μm (spinal cord). Myelination of peripheral nerves (F and G) (green arrowheads). (**H** and **I**) Nissl staining of P48 forebrain coronal sections. Scale bar, 1 mm. Insets show neocortical layers L1 to L6. Scale bar, 250 μm. (**J** to **L**) Quantification of Eri-C intensity in the forebrain (***$P = 0.0008$) (J), corpus callosum (CC) thickness [blue bracket in (H)] (**$P = 0.0016$) (K), and Nctx thickness [red bracket in (H)] ($P = 0.4776$) (L) in WT ($n = 3$) and *Tubb4a^Jit/Jit* ($n = 3$). Graphs represent means ± SD, each dot represents an animal, and significant differences are shown (Student's *t* test). A.U., arbitrary units. (**M** to **R**) Eri-C midsagittal staining at indicated stages from WT and *Tubb4a^Jit/Jit* animals. Scale bar, 5 mm. (**S** to **Z**) Cleaved caspase-3 (CASP3) immunohistochemistry (S, T, W, and X) and TEM (U, V, Y, and Z) on CC at P21 and P48 WT and *Tubb4a^Jit/Jit* animals. Red arrowheads indicate CASP3-positive cells. Scale bars, 50 μm (CASP3) and 2 μm (TEM). AC, anterior commissure; BG, basal ganglia; Nctx, neocortex; OT, olfactory tract; Str. Fasc., striatal fascicles.

progressively degenerated between P21 and P48 in *Tubb4a^Jit/Jit* mutants. To determine whether the loss of GCNs in *Tubb4a^Jit/Jit* mutants was caused by apoptosis, we performed CASP3 immunohistochemistry on tissue sections. CASP3-positive cells were present at both P21 and P35 in the IGL of *Tubb4a^Jit/Jit* mutants, while extremely rare in the IGL of WT animals (Fig. 2, J to N). CASP3-positive cells were present within the cerebellar white matter tracts, consistent with apoptotic OLs. Quantification showed an increase in apoptotic cells at P21 in *Tubb4a^Jit/Jit* mutants compared with WT and a highly significant increase at P35, consistent with the strong reduction of IGL size at that stage (Fig. 2N). CASP3 staining was not observed in other regions of the CNS except those associated with white matter tracts.

In *Tubb4a^Jit/Jit* mice, the ataxic motor phenotype was accompanied by a loss of GCNs; however, most human cerebellar ataxias associated with genetic mutations result from cerebellar Purkinje cell degeneration (*43*). To determine whether Purkinje cells were affected in *Tubb4a^Jit/Jit* mutants, we performed an immunohistological analysis using an anti-calbindin antibody to detect Purkinje cells. Purkinje cells were present in an organized monolayer in mutants similar to WT at P35 (fig. S2, C and D), suggesting that the *Jit* mutation strongly affected GCNs and not Purkinje cells. These data were also consistent with our observation that CASP-3 positive cells were rarely if at all detected in the PcL of both WT and *Tubb4a^Jit/Jit* animals (Fig. 2, L and M). These data were also consistent with the cerebellar pathology from patients with H-ABC, which revealed
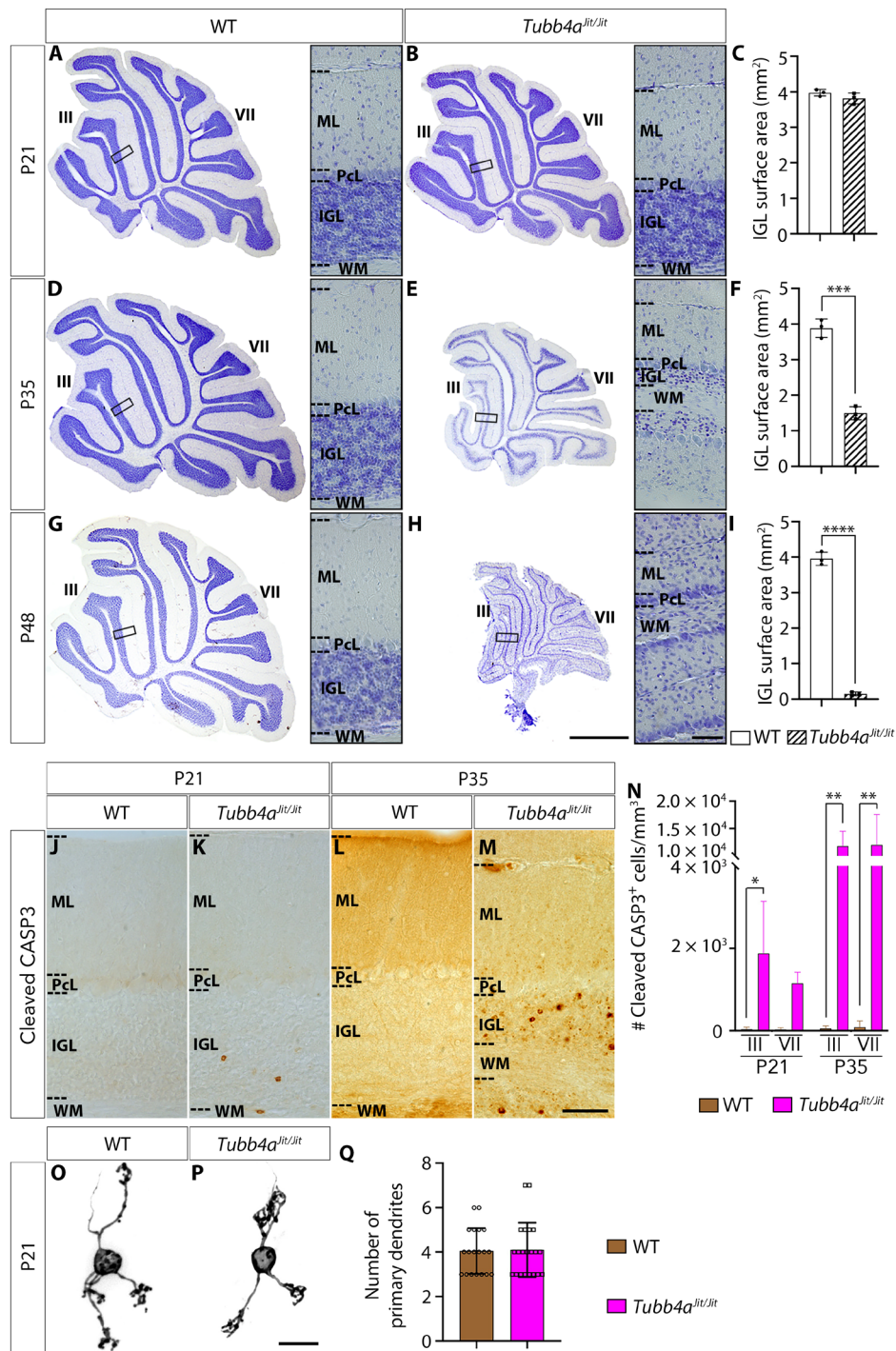
Fig. 2. Cerebellar GCNs degenerate in *Tubb4a*[Jit/Jit] mice. (**A** to **I**) Nissl staining (purple) of cerebellum midline sagittal sections and quantification of the IGL surface area in WT ($n = 3$) and *Tubb4a*[Jit/Jit] ($n = 3$) mice at P21 (A to C) ($P = 0.2013$), P35 (D to F) (***$P = 0.0002$), and P48 (G to I) (****$P < 0.0001$). Scale bar, 1 mm. Insets show higher magnification of the laminar structure of the cerebellum. Scale bar, 50 μm. Graphs represent means ± SD, each dot represents an animal, and significant differences are shown by asterisks (Student's t test). Lobules III and VII are noted by III and VII. (**J** to **M**) Cleaved CASP3 immunohistological staining (brown) on P21 (J and K) and P35 (L and M) cerebellum midline sagittal sections from WT and *Tubb4a*[Jit/Jit] mice. Scale bar, 50 μm. (**N**) Quantification of the number of CASP3-positive cells in lobule III and lobule VII of the cerebellum in WT ($n = 3$) and *Tubb4a*[Jit/Jit] ($n = 3$) mice at P21 and P35. P21 lobule III, WT versus *Tubb4a*[Jit/Jit], *$P = 0.0345$; P21 lobule VII, WT versus *Tubb4a*[Jit/Jit], $P = 0.2284$; P35 lobule III, WT versus *Tubb4a*[Jit/Jit], **$P = 0.0075$; P35 lobule VII, WT versus *Tubb4a*[Jit/Jit], **$P = 0.0068$. Graphs represent the means ± SD, and significant differences are shown by asterisks [one-way analysis of variance (ANOVA) followed by Tukey's for multiple comparisons]. (**O** and **P**) Dendritic morphology of cerebellar GCNs revealed by DiI retrograde tracing in WT (O) and *Tubb4a*[Jit/Jit] (P) mice at P21. Scale bar, 10 μm. (**Q**) Quantification of the number of primary dendrites in GCNs at P21 in WT and *Tubb4a*[Jit/Jit] mice ($P = 0.9061$). Graph represents the means ± SD, dots represent individual GCNs, and significant differences are shown by asterisks (Student's t test). IGL, inner granule cell layer; ML, molecular layer; PcL, Purkinje cell layer; WM, white matter.

atrophy of the cerebellar granule cell layer due to mutations in *TUBB4A* (*21*).

GCNs are small excitatory neurons that are essential components of the cerebellar circuit and are generated during mouse development from embryonic day 15.5 (E15.5) to ~P16 (*44–46*). The normal size and organization of the Cb in *Tubb4a*[*Jit/Jit*] mice at P21 therefore suggested that GCN production was not affected in the mutant. GCNs normally undergo a series of morphologically distinct stages of maturation within the IGL before acquiring their signature morphology characterized by four to five dendritic processes with elaborate "claws" that associate with ascending mossy fibers (*44*). To determine whether GCNs developed normally and matured after populating the IGL in the *Tubb4a*[*Jit/Jit*] mutants, we used DiI labeling to visualize the morphology of individual GCNs. DiI-labeled *Tubb4a*[*Jit/Jit*] GCNs had four to five dendritic processes characteristic of mature GCNs when labeled at P21 similar to WT, providing further evidence that the developmental program of GCN maturation was not affected in *Tubb4a*[*Jit/Jit*] mutants (Fig. 2, O to Q, and fig. S2, E and F). In sum, these results show that the cerebellum developed normally in *Tubb4a*[*Jit/Jit*] mutants in the absence of myelination, with mature GCNs present within the IGL, but subsequently, GCNs underwent a progressive degeneration and cell death through apoptosis, leading to the near disappearance of the IGL by P48.

The *Jittering* mutation causes dominant phenotypes in the CNS

Human tubulinopathies are nearly exclusively associated with de novo heterozygous missense mutations in tubulin isotype genes that result in amino acid substitutions, including patients with mutations in *TUBB4A* (*13*, *27*). This indicates that human disease-causing mutations act in a dominant manner. To determine whether the *Jit* mutation caused a dominant neural phenotype, we analyzed mice heterozygous for the *Jit* mutation. *Tubb4a*[*Jit/+*] animals did not exhibit the overt tremulous phenotype in young animals observed in homozygous mutants and lived a normal life span. However, heterozygotes did appear uncoordinated at advanced ages. We tested myelination in *Tubb4a*[*Jit/+*] animals using Eri-C staining. At P21, the *Tubb4a*[*Jit/+*] CNS showed abundant myelin; however, we detected a mild reduction compared with WT with a weaker Eri-C staining intensity in the anterior commissure, striatum, brainstem, and spinal cord (Fig. 3, A to H). The Cb size and cytoarchitecture of the *Tubb4a*[*Jit/+*] animals appeared similar to WT at P21. However, when aged to 1 year, *Tubb4a*[*Jit/+*] animals appeared grossly ataxic, and the *Tubb4a*[*Jit/+*] CNS showed a distinct reduction in Eri-C staining, revealing a progressive loss of myelin in *Tubb4a*[*Jit/+*] animals compared with WT (Fig. 3, I, J, and O). In addition, the Cb of the *Tubb4a*[*Jit/+*] mutants was reduced in size compared with WT with a significant reduction in the IGL surface area, indicating GCN degeneration (Fig. 3, K to N and P). To test whether myelination and cerebellar changes correlated with motor coordination deficits, we performed rotarod testing. *Tubb4a*[*Jit/+*] animals performed more poorly than WT littermates as early as P21, showing motor function deficits (Fig. 3Q). In addition, performance on the rotarod tests deteriorated markedly with increased age in *Tubb4a*[*Jit/+*] mutants compared with WT (Fig. 3, Q to T), while grip strength appeared unaffected, indicating that poor performance was not due to loss of strength (fig. S3). These results showed that *Tubb4a*[*Jit/+*] animals developed progressive myelin and cerebellar degeneration accompanied by a

deterioration in motor function, although following a less severe and slower time course than the *Tubb4a*[*Jit/Jit*] mutants. These results indicated that *Jit* mutation acted in a dominant fashion with a clear phenotype in heterozygotes.

Tubb4a is dispensable for neural development and homeostasis

Missense mutations such as N414K may act dominantly through haploinsufficiency or through dominant negative activity. Previous studies have shown that the heterozygote knockout of *Tubb4a* disrupted mitochondrial transport in neurons in vitro (*47*), raising the possibility that partial loss of function of *Tubb4a* might drive the dominant phenotypes in *Jit* mutants. To further study this issue, we generated a targeted knockout allele of *Tubb4a* (*Tubb4a*[*null*]) (fig. S4) and analyzed the mice on the FVB background. Unlike *Tubb4a*[*Jit/+*] mice that showed a progressive phenotype of cerebellar and myelin degeneration, *Tubb4a*[*null/+*] mice appeared unaffected with myelination, Cb size and cytoarchitecture, and rotarod performance, similar to those of WT mice through 1 year of age (Fig. 4, A, B, D to F, and H to K). The lack of a phenotype in *Tubb4a*[*null/+*] mice indicated that the *Jit* mutation did not cause dominant pathological changes through a loss of function. We next tested the requirement for *Tubb4a* by generating homozygous *Tubb4a*[*null/null*] knockout mice. Knockout animals did not develop the tremulous motor phenotypes of *Tubb4a*[*Jit/Jit*] mice nor did they appear ataxic at advanced age. Furthermore, *Tubb4a* knockout mice lived a similar life span as WT, and we failed to detect changes in Eri-C staining or cerebellum histology in *Tubb4a*[*null/null*] mice compared with WT controls through 1 year of age (Fig. 4, A to E, G, and H). We tested for motor coordination phenotypes by rotarod in *Tubb4a*[*null/null*] animals up to 1 year and found no significant differences in rotarod performance or grip strength compared with WT controls (Fig. 4, I to K, and fig. S4). These results showed that *Tubb4a* was neither required developmentally nor for myelination or Cb homeostasis. These results also indicate that the *Jittering* phenotype was not due to a loss of Tubb4a protein function, but rather a dominant activity of the Tubb4a[N414K] mutant protein.

We next performed a complementation test and crossed *Tubb4a*[*null/null*] mice with *Jit* heterozygotes to generate *Tubb4a*[*Jit/null*] animals. Although *Tubb4a* is not required in the mouse, the resulting compound heterozygotes exhibited gross motor phenotypes much stronger than in *Tubb4a*[*Jit/+*] mice and almost as severe as in *Jit* homozygous mutants, although the phenotypes developed more slowly (Fig. 5). These results showed that the alleles failed to complement. *Tubb4a*[*Jit/null*] compound heterozygotes variably survived up to ~14 weeks with motor defects similar to *Tubb4a*[*Jit/Jit*] mutants at end stage (P48). At P95, *Tubb4a*[*Jit/null*] compound heterozygotes exhibited reduced white matter tracts (e.g., CC, anterior commissures, and striatal fascicles) and a strongly diminished Eri-C staining, indicating reduced myelin (Fig. 5, K, L, P, and Q) similar to *Tubb4a*[*Jit/Jit*] mutants at P48 (Fig. 1, D and E). Moreover, at P95, *Tubb4a*[*Jit/null*] mutants had a severely atrophic cerebellum (Fig. 5, M to O) with the IGL layer largely devoid of GCNs, similar to *Tubb4a*[*Jit/Jit*] mutants at P48. The cerebellum was also severely demyelinated (Fig. 5, R to T). However, at P48, the myelination and cerebellar phenotypes of the *Tubb4a*[*Jit/null*] compound heterozygotes were less severe than at P95 and were also less severe than in the *Tubb4a*[*Jit/Jit*] mutants assayed at P48 (Fig. 5, A to J). At P48, the *Tubb4a*[*Jit/null*] compound heterozygotes displayed a reduction in myelin and Cb size, but it
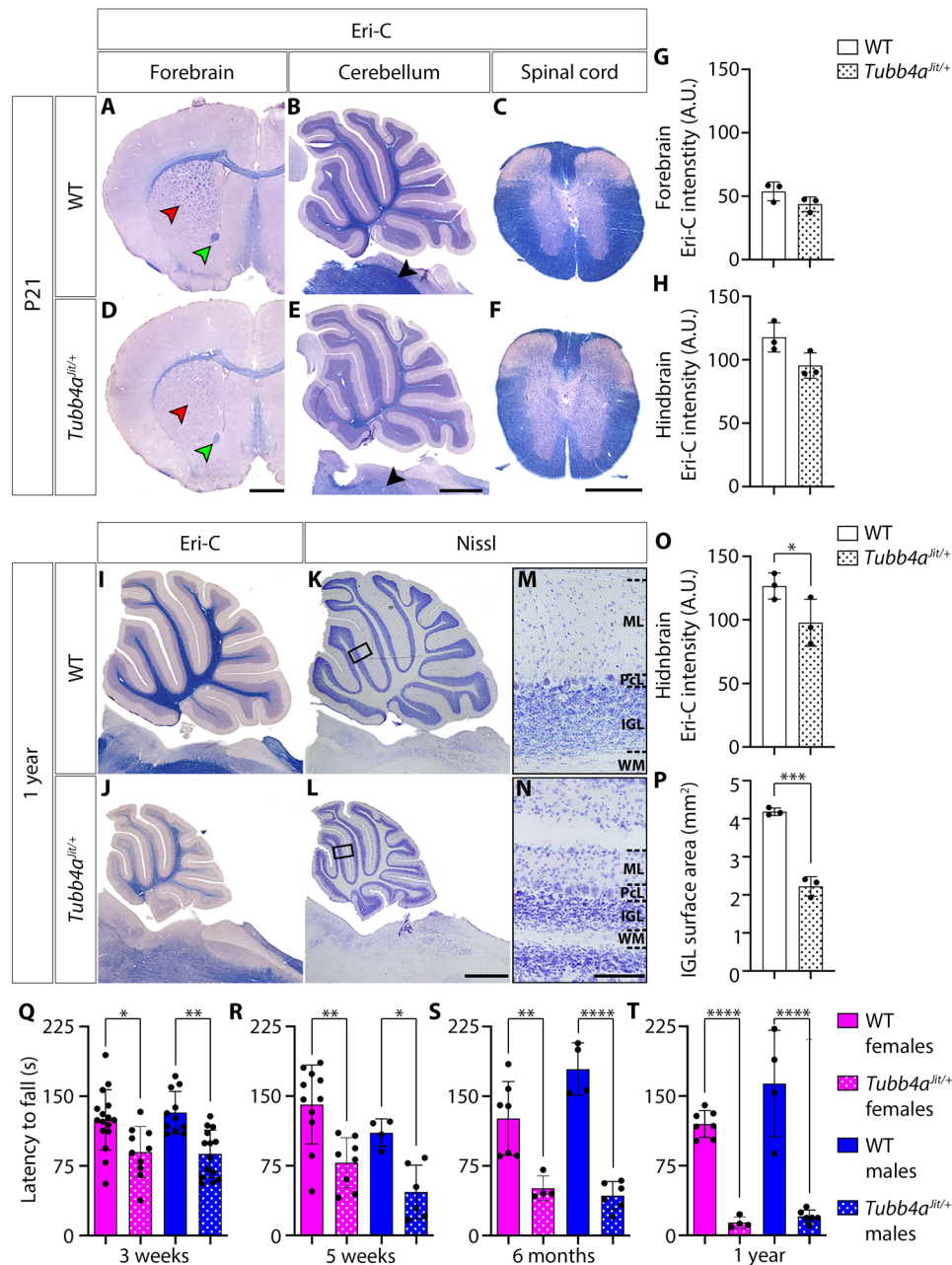
Fig. 3. *Jittering* mutation acts dominantly. (**A** to **F**) Eri-C staining of myelin (blue) of P21 forebrain coronal sections (A and D), hindbrain midsagittal sections (B and E), and spinal cord coronal sections (C and F) from WT and *Tubb4a^{Jit/+}* mouse CNS showing a general reduction of myelination most visible in the brainstem (black arrowheads), anterior commissures (green arrowheads), and striatal fascicles (red arrowheads) in the *Tubb4a^{Jit/+}* compared with WT mice. Scale bars, 1 mm (A, B, D, and E) and 500 μm (C and F). (**G** and **H**) Quantification of Eri-C staining intensity in the forebrain (*P* = 0.1367) (G) and hindbrain (*P* = 0.0661) (H) of WT (*n* = 3) and *Tubb4a^{Jit/+}* (*n* = 3) mice at P21. (**I** to **N**) Hindbrain midline sagittal sections stained for Eri-C (I and J) and Nissl (K to N) from 1-year-old WT and *Tubb4a^{Jit/+}* mice. Scale bars, 1 mm (I to L) and 100 μm (M and N). (**O**) Quantification of Eri-C staining intensity in the hindbrain of WT (*n* = 3) and *Tubb4a^{Jit/+}* (*n* = 3) mice at 1 year (**P* = 0.0295). (**P**) Quantification of IGL surface area in cerebellum of WT (*n* = 3) and *Tubb4a^{Jit/+}* (*n* = 3) mice at 1 year (****P* = 0.0002). (G, H, O, and P) Graphs represent the means ± SD, with dots representing individual animals and significant differences by asterisks (Student's *t* test). (**Q** to **T**) Rotarod performance measured by the latency to fall in seconds (s) of WT and *Tubb4a^{Jit/+}* female and male mice at 3 weeks (**P* = 0.0176 and ***P* = 0.0014) (Q), 5 weeks (***P* = 0.0025 and **P* = 0.0321) (R), 6 months (***P* = 0.0027 and *****P* < 0.0001) (S), and 1 year (*****P* < 0.0001) (T). Graphs represent the means ± SD, with each dot representing an animal. Two-way ANOVA (Tukey's multiple comparisons test).

was not as severe as in the *Tubb4a^{Jit/Jit}* animals (Fig. 5, C to G, and Fig. 1, D, E, and G to I), and CC thickness was less reduced in the *Tubb4a^{Jit/null}* compound heterozygotes than in the *Tubb4a^{Jit/Jit}* animals (Fig. 1E, I and Fig. 5B, G). The analysis of the myelin and Cb phenotype of the *Tubb4a^{Jit/null}* compound heterozygotes at P48

and P95 therefore showed a progressive degeneration of myelin and GCNs. Thus, the phenotype of *Tubb4a^{Jit/null}* compound heterozygotes, while more slowly developing than that of the *Tubb4a^{Jit/Jit}* animals, was much stronger than that of the *Tubb4a^{Jit/+}* animals. In sum, these studies showed that loss of Tubb4a function did not
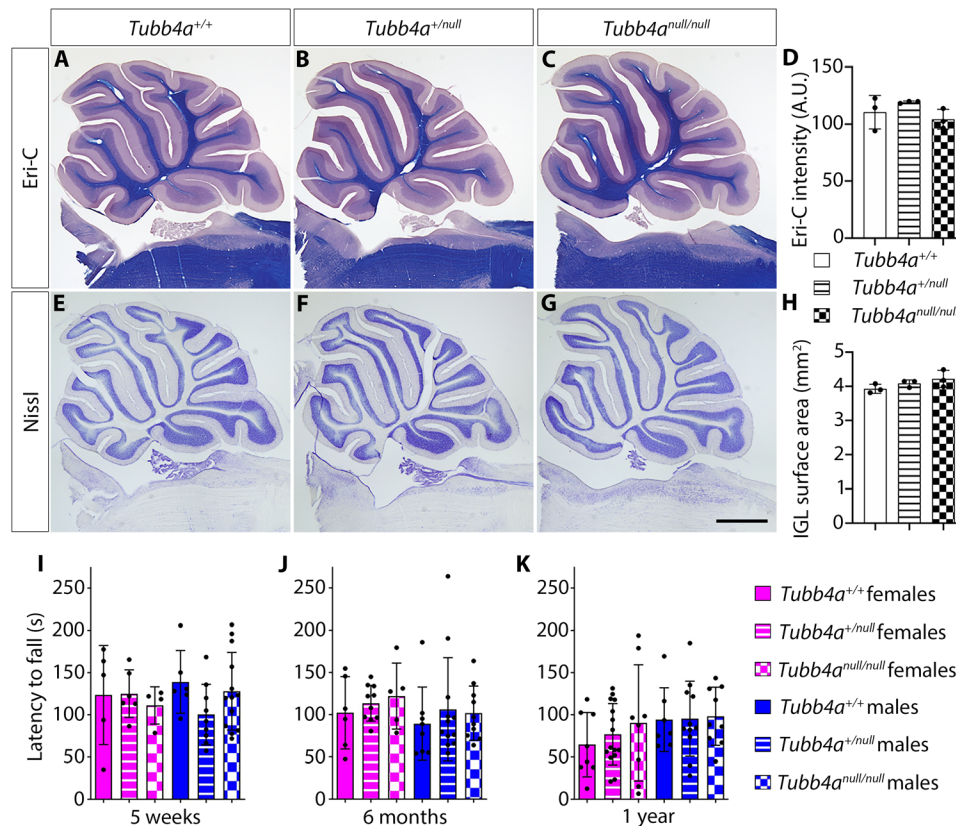
Fig. 4. *Tubb4a* is not required for myelination or cerebellar homeostasis. (**A** to **C**) Eri-C staining (blue) of hindbrain sagittal midline sections of 1-year-old WT, *Tubb4a*$^{null/+}$, and *Tubb4a*$^{null/null}$ mice. (**D**) Quantification of Eri-C staining intensity in hindbrains of WT ($n = 3$), *Tubb4a*$^{+/null}$ ($n = 3$), and *Tubb4a*$^{null/null}$ ($n = 3$) mice. (WT versus *Tubb4a*$^{+/null}$, $P = 0.5495$; WT versus *Tubb4a*$^{null/null}$, $P = 0.7320$; *Tubb4a*$^{+/null}$ versus *Tubb4a*$^{null/null}$, $P = 0.2269$). (**E** to **G**) Nissl staining of hindbrain sagittal midline sections of 1-year-old WT, *Tubb4a*$^{null/+}$, and *Tubb4a*$^{null/null}$ mice. Scale bar, 1 mm. (**H**) Quantification of IGL surface area in cerebellum of WT ($n = 3$), *Tubb4a*$^{+/null}$ ($n = 3$), and *Tubb4a*$^{null/null}$ ($n = 3$) mice (WT versus *Tubb4a*$^{+/null}$, $P = 0.5575$; WT versus *Tubb4a*$^{null/null}$, $P = 0.1882$; *Tubb4a*$^{+/null}$ versus *Tubb4a*$^{null/null}$, $P = 0.6393$). Graphs represent the means ± SD, with each dot representing an animal (one-way ANOVA followed by Tukey's multiple comparisons test). (**I** to **K**) Rotarod performance measured as the latency to fall in seconds (s) of WT, *Tubb4a*$^{null/+}$, and *Tubb4a*$^{null/null}$ female and male mice at 5 weeks (I), 6 months (J), and 1 year (K). Graphs represent the means ± SD, with each dot representing each individual animal. No significant changes were detected (two-way ANOVA followed by Tukey's multiple comparisons test; significance was considered achieved for $P < 0.05$).

underlie the dominant pathological phenotypes observed in *Tubb4a*^{Jit} animals as mice null for *Tubb4a* did not show neural or motor phenotypes. However, the loss of the WT *Tubb4a* allele in mice strongly exacerbated the *Tubb4a*^{Jit} heterozygous phenotype.

Deletion of the WT *Tubb4a* allele cell-autonomously exacerbates *Tubb4a*$^{Jit/+}$ phenotypes

Myelination is essential to support neuronal function, and deficits in myelin result in axonal damage and neuronal death, raising the possibility that the developmental defects in myelinating cells could cause disruption in cerebellar development and homeostasis. In addition, GCN function is dependent on the association with myelinated ascending axons of their main afferents, the mossy fibers. We sought to determine the relationship between GCN degeneration and myelination in *Jit* mice through genetic methods. We took advantage of the stronger phenotype of the *Tubb4a*$^{Jit/null}$ mice compared with *Tubb4a*$^{Jit/+}$ to use a conditional approach to determine whether the *Jit* mutation acts cell autonomously to cause cerebellar cell death. We used a floxed allele of *Tubb4a* (*Tubb4a*^{fl}) (fig. S4) to delete *Tubb4a* in either the oligodendrocyte or GCN lineages on the *Jit* heterozygous background

(*Tubb4a*$^{Jit/fl}$ animals). Deletion of the floxed allele would create *Tubb4a*$^{Jit/null}$ in cells where cre is expressed that would exhibit a stronger cellular phenotype than the *Tubb4a*$^{Jit/fl}$ cells that did not express cre. We generated *Tubb4a*$^{Jit/fl}$ mice carrying the *NG2-cre* allele (*NG2-cre;Tubb4a*$^{Jit/fl}$ conditional knockout mice or *NG2-cKO*) (*48*), which expresses cre in oligodendrocyte precursors. We compared their cerebellar and myelination phenotypes to *Tubb4a*$^{Jit/fl}$ mice that did not carry *NG2-cre* at 4 months of age. We found that *NG2-cKO* mice showed greatly diminished Eri-C staining compared with *Tubb4a*$^{Jit/fl}$ mice (Fig. 6, A to C), as expected. However, the IGL surface area was not significantly affected (Fig. 6, D to F). These results indicated that loss of myelination did not significantly affect GCN survival.

Conversely, we tested whether loss of GCNs influenced myelination. We generated *Tubb4a*$^{Jit/fl}$ mice carrying *Atoh1-cre* (*Atoh1-cre;Tubb4a*$^{Jit/fl}$ conditional knockout mice or *Atoh1-cKO*), which is expressed in the cerebellar granule cell progenitors (*49*), and compared these mice with *Tubb4a*$^{Jit/fl}$ mice that lacked *Atoh1-cre*. We analyzed midsagittal sections through the Cb and brainstem at 6 months and found a marked loss of GCNs in the *Atoh1-cKO* mice compared with
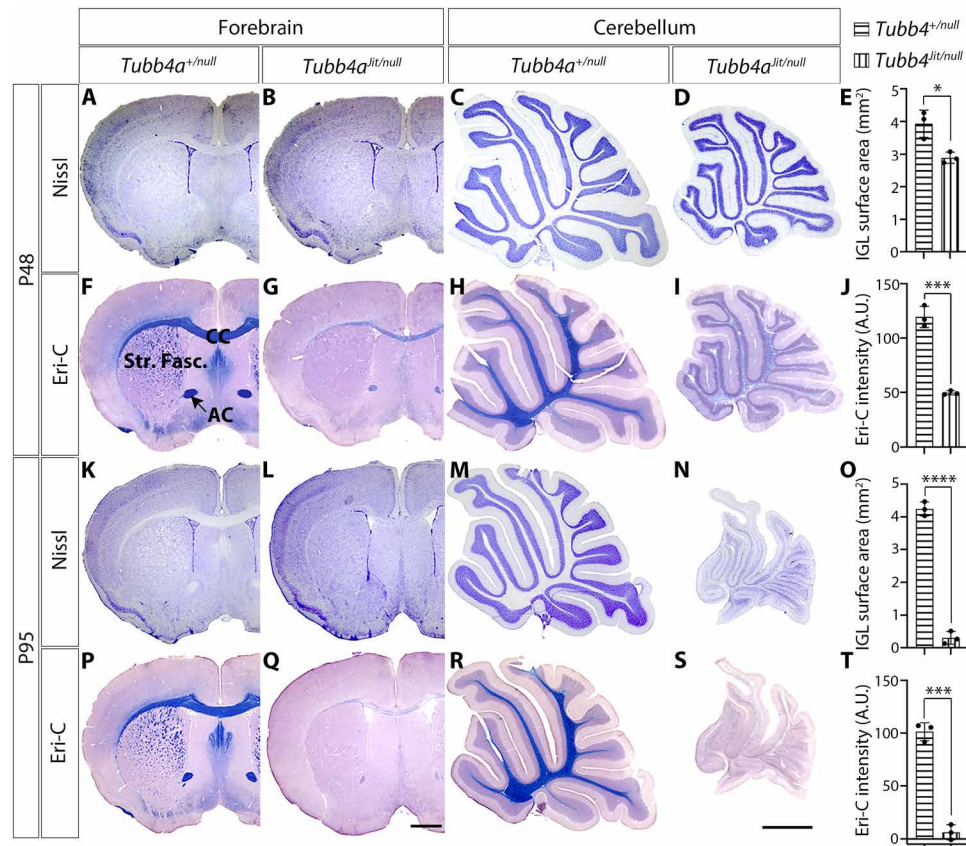
Fig. 5. *Tubb4a^{Jit/null}* mice display strong cerebellar and myelin defects. (**A** to **D**) Nissl staining of forebrain coronal sections (A and B) and cerebellum midline sagittal section (C and D) from *Tubb4a^{+/null}* and *Tubb4a^{Jit/null}* mice at P48. (**E**) Quantification of IGL surface area (*P = 0.0159) of *Tubb4a^{+/null}* (n = 3) and *Tubb4a^{Jit/null}* (n = 3) cerebellum at P48. (**F** to **I**) Eri-C staining of forebrain coronal sections (F and G) and cerebellum midline sagittal section (H and I) from *Tubb4a^{+/null}* and *Tubb4a^{Jit/null}* mice at P48. (**J**) Quantification of Eri-C staining intensity in the hindbrain (***P = 0.0003) in *Tubb4a^{+/null}* (n = 3) and *Tubb4a^{Jit/null}* (n = 3) mice at P48. (**K** to **N**) Nissl staining of forebrain coronal sections (K and L) and cerebellum midline sagittal section (M and N) from *Tubb4a^{+/null}* and *Tubb4a^{Jit/null}* mice at P95. (**O**) Quantification of IGL surface area (****P < 0.0001) of *Tubb4a^{+/null}* (n = 3) and *Tubb4a^{Jit/null}* (n = 3) cerebellum at P95. (**P** to **S**) Eri-C staining of forebrain coronal sections (P and Q) and cerebellum midline sagittal section (R and S) from *Tubb4a^{+/null}* and *Tubb4a^{Jit/null}* mice at P95. (**T**) Quantification of Eri-C staining intensity in the hindbrain (***P = 0.0001) in *Tubb4a^{+/null}* (n = 3) and *Tubb4a^{Jit/null}* (n = 3) mice at P95. Graphs represent the means ± SD, dots represent individual mice, and significant differences are shown by asterisks (Student's t test). Scale bars, 1 mm.

Tubb4a^{Jit/fl} mice (Fig. 6, J to L), as expected. Notably, myelin levels in the cerebellum and brainstem of *Atoh1-cKO* mice were similar to those of *Tubb4a^{Jit/fl}* mice that did not express cre (Fig. 6, G to I), showing that the *Tubb4a^{Jit}* mutation in GCNs is sufficient to trigger GCN degeneration and the degeneration of cerebellar GCNs occurred independently of myelin status. Together, these results indicated that the *Tubb4a^{Jit}* mutation caused GCN degeneration and myelination defects independently through cell-autonomous mechanisms.

Tubb4a is expressed broadly in the CNS
MTs are ubiquitous; yet, tubulinopathies display distinct tissue phenotypes in patients, and, similarly, only specific cell types were affected in *Jit* mutants. To better understand how the *Jit* mutation caused specific pathological changes in the CNS, we determined the expression pattern of *Tubb4a* during development. We performed in situ hybridization using an antisense riboprobe specific for *Tubb4a*. At P3, little or no expression was found in the brain (Fig. 7, A, D, and E). Expression levels increased markedly in the ensuing days, and by P10, we observed a broad expression of

Tubb4a in most regions of the CNS that became stronger by P21 (Fig. 7, B to E). White matter tracts such as the CC contained *Tubb4a*-expressing cells, indicating expression by oligodendrocytes (Fig. 7D). Within the developing cerebellum, *Tubb4a* was expressed by cells in the IGL and cells in the cerebellar white matter tracts, consistent with expression in cerebellar GCNs and oligodendrocytes (Fig. 7E). Notably, *Tubb4a* expression was absent in the external granule layer (EGL) at P10, the site where GCN progenitors proliferate before exiting the cell cycle and migrating to their final position within the IGL (Fig. 7E). This indicated that *Tubb4a* was not expressed in the mitotic GCN progenitors but in differentiated GCNs. *Tubb4a* expression was also not restricted to oligodendrocytes and GCNs, the two cell types strongly affected in *Jit* animals, as *Tubb4a* expression was observed broadly in neural cells throughout the brain and brainstem (Fig. 7). In control experiments, no expression was detected using the *Tubb4a* in situ probe in *Tubb4a^{null/null}* brains at all ages tested (fig. S6). These in situ data are also consistent with the tissue expression of *Tubb4a* using polymerase chain reaction (PCR) approaches (*7*, *32*) and show that *Tubb4a* was widely expressed throughout the CNS.
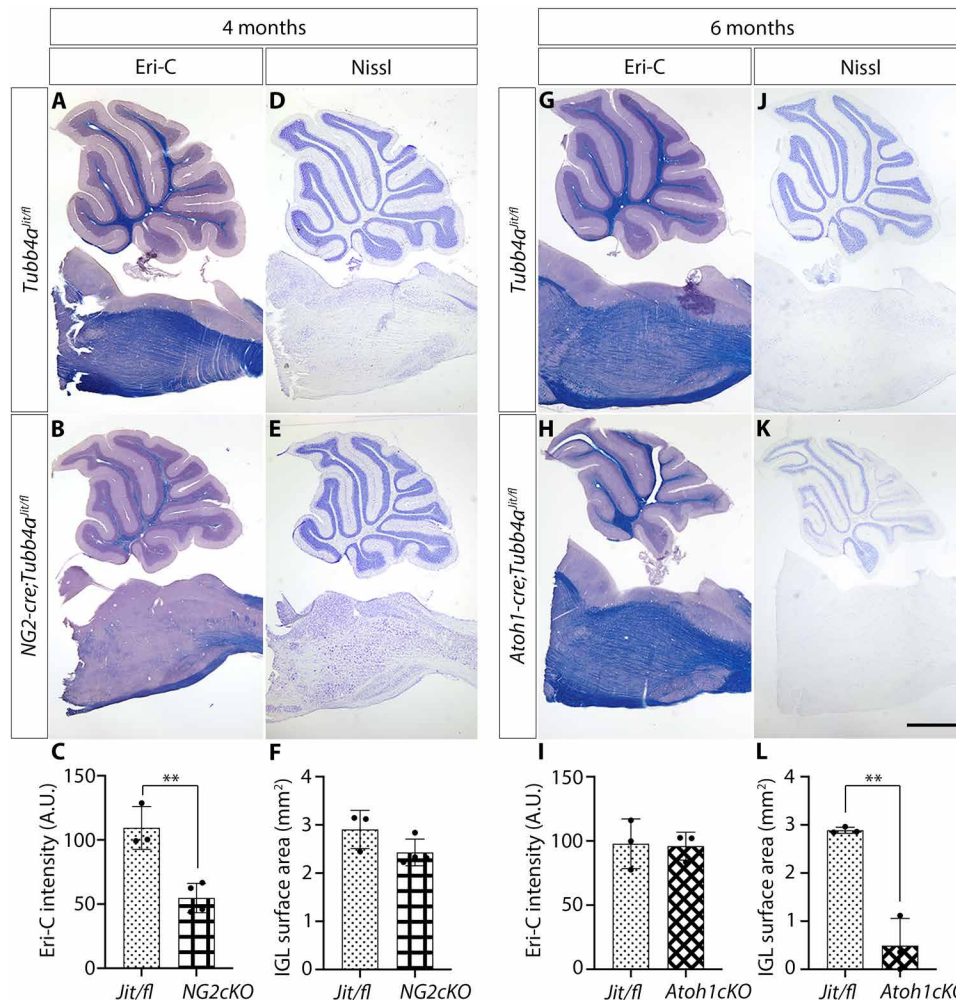
Fig. 6. Deletion of the WT *Tubb4a* allele cell-autonomously exacerbates *Tubb4a^Jit/+* phenotypes. (**A** to **F**) Analysis of the phenotype of *NG2-Cre;Tubb4a^Jit/fl* conditional knockout (NG2-cKO) compared to *Tubb4a^Jit/fl* animals at 4 months. Eri-C staining of hindbrain midsagittal sections (A and B) and quantification of the intensity of Eri-C staining in hindbrains (C) of *Tubb4a^Jit/fl* (n = 3) and *NG2-cKO* (n = 4) animals showing a clear reduction of myelination levels in *NG2-cKO* animals compared with *Tubb4a^Jit/fl* animals (**P = 0.0035). Nissl staining of hindbrain midsagittal sections (D and E) and quantification of the surface area of IGL (P = 0.1181) (F) in the cerebellum from *Tubb4a^Jit/fl* (n = 3) and *NG2-cKO* (n = 4) mice. (**G** to **L**) Analysis of the phenotype of *Atoh1-Cre;Tubb4a^Jit/fl* conditional knockout (*Atoh1-cKO*) animals compared with *Tubb4a^Jit/fl* animals at 6 months. Eri-C staining of hindbrain midsagittal sections (G and H) and quantification of the intensity of Eri-C staining in the hindbrain (I) of *Tubb4a^Jit/fl* (n = 3) and *Atoh1-cKO* (n = 3) brains, showing no reduction of myelination levels in *Atoh1-cKO* animals compared with *Tubb4a^Jit/fl* animals (P = 0.8938). Nissl staining of hindbrain midsagittal sections of *Tubb4a^Jit/fl* and *Atoh1-cKO* brains (J and K) and quantification of the surface area of IGL (L) showing a strong reduction of the IGL in the *Atoh1-cKO* animals (n = 3) compared with *Tubb4a^Jit/fl* animals (n = 3)(**P = 0.0019). Graphs represent the means ± SD, dots represent individual mice, and significant differences are shown by asterisks (Student's *t* test).

Phenotypic severity correlates with the expression ratio of *Tubb4a^Jit* relative to other β-tubulin isotypes

The broad expression of *Tubb4a* in the CNS raised the question of why GCNs and oligodendrocytes were disrupted in *Jit* mutants while other cell types appeared unaffected. During MT assembly, monomeric β-tubulin proteins present in intracellular pools heterodimerize in an obligate 1:1 ratio with α-tubulins before incorporation (*50*). The representation of Tubb4a in MTs therefore depends on its abundance relative to other β-tubulins present in the cell, which could compete for incorporation into MT. We found that Tubb4a^N414K mutant protein is readily incorporated into MTs, as expression of C-terminal hemagglutinin (HA)–tagged Tubb4a^N414K in cells revealed HA immunoreactivity in MT similar to HA-tagged

WT Tubb4a protein (fig. S7) and consistent with studies of the identical mutation in the human gene (*21*) and previous studies of amino acid substitutions in the H12 of β-tubulin (*51*), the domain where the *Jit* mutation resides. We therefore hypothesized that the phenotypic strength of the dominant-acting *Jit* mutation depended on the proportion of its expression in relation to all β-tubulin expression in the cells. We sought to evaluate the relative abundance of tubulin-β4a by examining the expression levels of the eight β-tubulin genes in the mouse at P21. We performed this analysis using quantitative PCR (qPCR) as tubulin isotype–specific antibodies have not been developed for most isotype proteins. We microdissected the CC, which is highly enriched with the cell bodies of oligodendrocytes, and the cerebellar IGL, which is tightly packed with GCNs, as
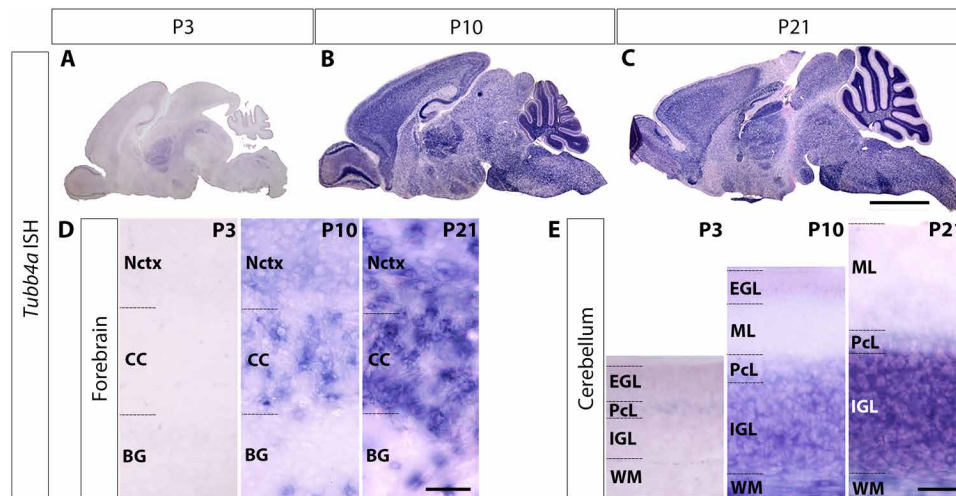
Fig. 7. *Tubb4a* is broadly expressed in the CNS. In situ hybridization (ISH) against *Tubb4a* mRNA on midsagittal sections of the brain of WT mice at P3 (**A**), P10 (**B**), and P21 (**C**). Scale bar, 2 mm. High magnification of the forebrain at the border of the Nctx, CC, and BG (**D**), and of the cerebellum (**E**). (D and E) Scale bars, 50 μm.

these two cell types were strongly affected and at the origin of the phenotypes observed in *Jit* mutants. Notably, in the WT CC and IGL, *Tubb4a* mRNA was highly abundant among the β-tubulin mRNAs and represented ~60% of the total β-tubulin mRNAs expressed (Fig. 8A). For comparison, we dissected the ML of the cerebellum, which contains cerebellar interneurons at P21, and the neocortical layers 1 to 3, which are enriched for the cell bodies of cortical projection neurons at P14, cell types that appeared histologically unaffected by the *Jit* mutation. *Tubb4a* was expressed in the ML and WT neocortical layers 1 to 3, but its relative abundance was considerably lower in these tissues than in CC and IGL and comprised only ~20 to 22% of the total β-tubulin transcripts (Fig. 8A). The qPCR data were consistent with RNA sequencing (RNA-seq) studies that showed *Tubb4a* constituted the majority of β-tubulin transcripts in differentiated oligodendrocytes (fig. S8A), but only a minor percentage in cortical neurons (fig. S8, A and B) (*52, 53*). In addition, RNA-seq studies showed that the expression ratio of *Tubb4a* was relatively low in other cell types that were grossly unaffected in *Jit*, including oligodendrocyte precursors, astrocytes, microglia, and endothelial cells (fig. S8A) (*52*). These results showed that *Tubb4a* transcription was proportionally high among the total expression of β-tubulins in neural tissues affected by *Jit* mutation, while other cell types expressed much lower relative levels of *Tubb4a*.

Tubb4a represented ~60% of the total β-tubulin transcripts in oligodendrocytes and GCNs, yet we failed to detect a phenotype in *Tubb4a^null^* mice. We therefore examined whether expression of β-tubulin isotype genes was altered in *Tubb4a^null^* mice to compensate for the loss of *Tubb4a*. In the *Tubb4a^null/null^* CC, we found transcriptional up-regulation of most β-tubulins, including significantly higher levels of *Tubb2a*, *Tubb2b*, and *Tubb5* compared with WT, which indicated that in *Tubb4a^null/null^* mutant oligodendrocytes, multiple β-tubulins compensated for the loss of *Tubb4a* (Fig. 8A). In the *Tubb4a^null/null^* IGL region of the cerebellum, we found that *Tubb2a* transcription was strongly up-regulated from ~7% in WT to ~60% of the total β-tubulins, indicating compensation was, in large part, from a single tubulin gene in GCNs (Fig. 8B). Total β-tubulin levels were not significantly changed in *Tubb4a^null/null^* mutants

compared with WT in the tissues tested (Fig. 8B). These data were consistent with the idea that β-tubulin isotype proteins could functionally compensate for the loss of *Tubb4a* and that transcriptional compensation was cell type dependent.

We next determined the levels of mutant *Tubb4a^Jit^* transcription among β-tubulins in the *Jit* allelic series. In the IGL of *Tubb4a^Jit/Jit^* mice, we found that mutant *Tubb4a* represented ~60% of the total β-tubulin mRNAs, similar to the proportion of *Tubb4a* expression among total β-tubulins in WT controls (Fig. 8A). This indicated that mutant *Tubb4a^Jit^* made up a large proportion of total β-tubulin expression in *Tubb4a^Jit/Jit^* mutant IGL. We next examined the relative levels of expression of the various tubulin genes in *Tubb4a^Jit/null^* mice. One might have expected *Tubb4a^Jit/null^* mice to have a similar phenotype as *Tubb4a^Jit/+^* as both harbor a single copy of the dominant-acting *Jit* allele and that *Tubb4a* is redundant and not required in the mouse. Instead, *Tubb4a^Jit/null^* mice exhibited a very strong phenotype when compared with *Tubb4a^Jit/+^* animals, but more slowly developing than *Tubb4a^Jit/Jit^* mutants (Fig. 5). We found that *Tubb4a^Jit^* transcripts represented ~50% of total β-tubulin transcripts in the IGL of *Tubb4a^Jit/null^* animals (Fig. 8A), which was a significant reduction (*P* < 0.0001) compared with the ~60% in the *Tubb4a^Jit/Jit^* animals. However, this was a much higher level than the predicted ~30% present in *Tubb4a^Jit/+^* animals, assuming the WT and mutant loci are equally transcribed. These results are consistent with a model that deletion of the WT allele in *Tubb4a^Jit^* heterozygotes worsened the phenotype by increasing the expression ratio of the mutant *Tubb4a^Jit^* with respect to the other β-tubulins expressed. Again, total β-tubulin transcript levels were not significantly altered in the IGL harboring the *Tubb4a^Jit^* or *Tubb4a^null^* alleles (Fig. 8B). These results indicated that the severity of the neural phenotypes in mutants of the *Jit* allelic series correlated with the relative abundance of *Tubb4a^Jit^* transcription within the β-tubulin family. These data were consistent with a model that the origin and strength of cell-specific pathologies in the *Jit* allelic series were due to the proportional abundance of a dominant-acting mutant tubulin species with regard to the β-tubulin family members (Fig. 9).
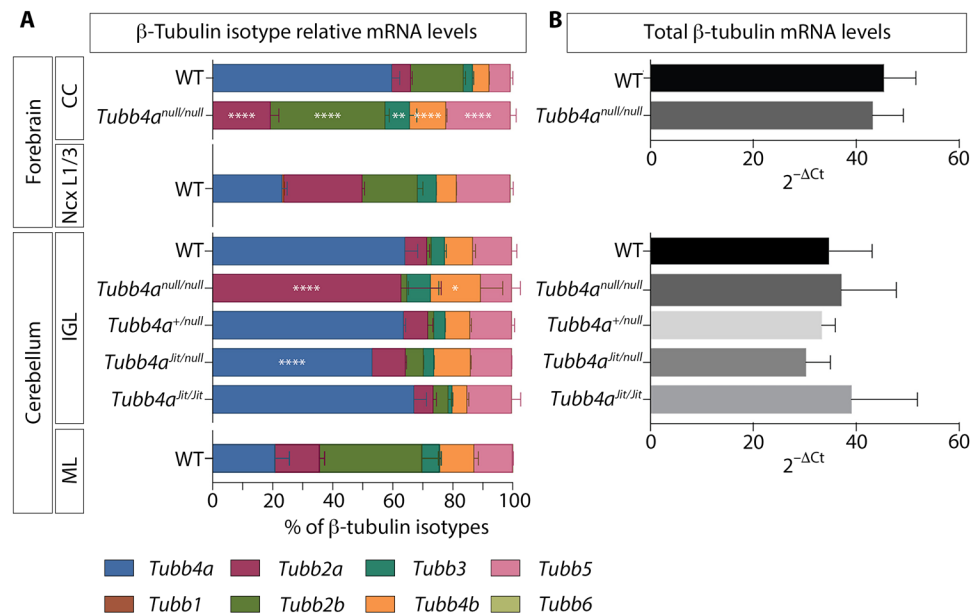
Fig. 8. Expression ratios of β-*tubulin* isotype mRNA in the *Tubb4a* allelic series. (**A**) Relative abundance of the eight murine β-*tubulin* isotype transcripts assessed by reverse transcription qPCR in the forebrain [CC (P21) and neocortical superficial layers 1 to 3 (NcxL1/3; P14)] and in the cerebellum [IGL (P21) and ML (P21)], dissected from mice of the *Tubb4a* allelic series of the indicated genotypes. In the CC, β-tubulin isotype mRNAs from *Tubb4a*^null/null^ (n = 3) mice were compared with β-tubulin isotype mRNAs from WT (n = 3) mice (**P = 0.0012 and ****P < 0.0001), and in the IGL, β-tubulin isotype mRNAs from *Tubb4a*^null/null^ (n = 3), *Tubb4a*^+/null^ (n = 3), *Tubb4a*^Jit/null^ (n = 3), and *Tubb4a*^Jit/Jit^ (n = 3) mice were compared with β-tubulin isotype mRNAs from WT (n = 3) mice (*P = 0.0121 and ****P < 0.0001). Graphs represent the mean percentage ± SEM (two-way ANOVA followed by Tukey's multiple comparisons test). (**B**) Total β-tubulin mRNA levels in the forebrain (CC) and cerebellum (IGL) of the indicated genotypes. Graphs represent means of $2^{-\Delta Ct}$ ± SEM. Comparisons showed no significance differences (one-way ANOVA).

DISCUSSION

Jittering mutation and Tubb4a-associated diseases
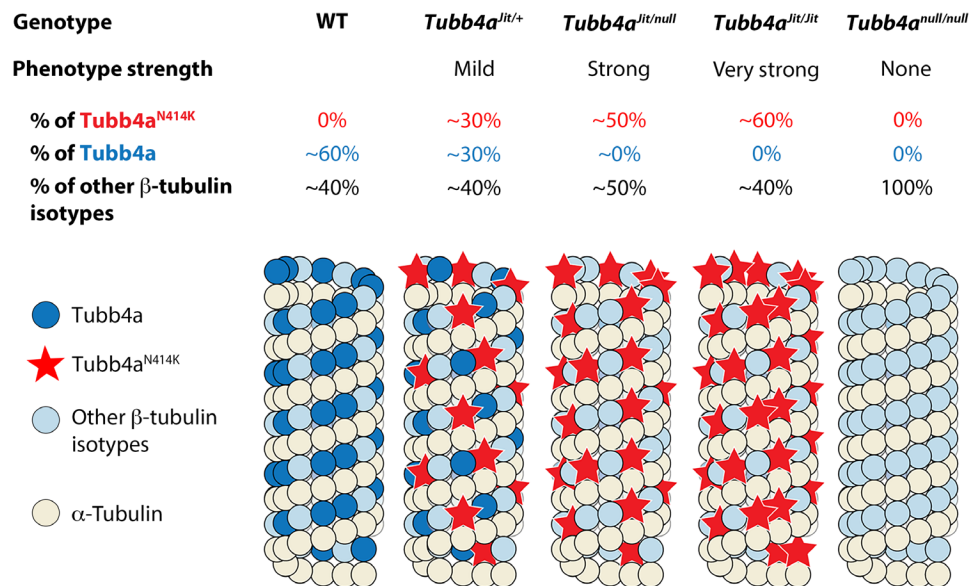
We identified a dominant missense mutation (N414K) in the β-tubulin isotype gene *Tubb4a* that causes dominant degenerative phenotypes affecting cerebellar GCNs and oligodendrocytes. Tubulin isotype genes are highly homologous, and the *Jit* missense (N414K) lies within the tubulin H12 and introduces a positively charged lysine into this negatively charged region of the protein that faces externally on the MT barrel. H12 is known to serve as an interface on the MT surface that interacts with kinesin motors. Multiple studies have shown that amino acid substitutions within the H12 domain adversely affects kinesin binding and movement (*51*, *54*, *55*). Amino acid substitutions that introduced positively charged residues into H12 were previously found to be particularly disruptive to kinesin-MT interactions (*54*). TUBB4A^N414K^ mutant protein in vitro showed that the mutation affected neither tubulin stability nor its ability to be incorporated into MTs; however, MTs containing the TUBB4A^N414K^ had altered dynamics (*21*). TEM analysis of CNS tissue from a patient with H-ABC that harbored the identical N414K mutation in human TUBB4A showed more numerous MTs in oligodendrocytes (*20*), consistent with the idea that disease-causing mutations in tubulins cause disease by altering MT dynamics (*12*, *56*).

In patients, mutations in *TUBB4A* are associated with a spectrum of CNS disorders including primary dystonia DYT4/whispering dysphonia (OMIM 128101) and hypomyelination with variable cerebellar or basal ganglia involvement (*27*). In addition, a patient with H-ABC that was identified to harbor the identical N414K amino acid substitution in *TUBB4A* displayed severe hypomyelination and cerebellar GCN degeneration in an early encephalopathic variant form of the disease (*20*, *21*), a similar pathology as observed in *Jit*

mutant mice. The spectrum of human diseases associated with *TUBB4A* are all caused by heterozygous missense mutations. *Jit* therefore serves as a murine model for the encephalopathic variant form of H-ABC and also phenocopies the dominant inheritance and neuropathology of this rare genetic disorder. Mutations causing amino acid substitutions in different regions of the human TUBB4A protein appear to result in phenotypes of varying onset and clinical severity (*27*). Consistent with these observations, the spontaneous rat mutation *taiep* results in a milder, recessive phenotype compared to *Jit*. The *taiep* phenotype is caused by an A302T missense located in a region of TUBB4A involved in mediating lateral interactions between α/β-tubulin heterodimers that affects myelination but not cerebellar granule cells (*20*). Recently, a mouse harboring a D249N missense and serving as a model of the most common form of H-ABC reported a recessive motor phenotype accompanied by degeneration of myelin and the cerebellum (*42*). In contrast, the *Jit* mutation displayed dominant degenerative phenotypes present in heterozygote mice, similar to the hypomyelination and cerebellar atrophy present in patients with H-ABC and consistent with disruption of MT function.

An expression ratio model of tubulinopathy

There has been recent interest in the functional roles of the multiple tubulin isotype genes, and evidence is building that tubulin isotype composition participates in generating a tubulin code that determines MT properties (*26*, *27*, *35*). Because MTs are ubiquitous structures involved in a myriad of cellular functions, the existence of the code has broad significance for cellular physiology and for understanding the basis of the multiple genetic tubulinopathies. MT properties are determined by their tubulin isotype composition and posttranslational

Genotype	WT	*Tubb4a*$^{Jit/+}$	*Tubb4a*$^{Jit/null}$	*Tubb4a*$^{Jit/Jit}$	*Tubb4a*$^{null/null}$
Phenotype strength		Mild	Strong	Very strong	None
% of Tubb4a^{N414K}	0%	~30%	~50%	~60%	0%
% of Tubb4a	~60%	~30%	~0%	0%	0%
% of other β-tubulin isotypes	~40%	~40%	~50%	~40%	100%

● Tubb4a

★ Tubb4a^{N414K}

● Other β-tubulin isotypes

○ α-Tubulin

Fig. 9. Phenotypic strength correlates with expression ratio of *Tubb4a*. This model shows predicted protein levels in MTs of cerebellar GCNs, assuming mRNA levels translate into similar protein levels in MTs. We propose that the abundance of *Jit* mutant Tubb4a (Tubb4a^{N414K}) protein in MTs, based on *Tubb4a*^{Jit} transcript expression ratio among β-tubulin transcripts, defines the strength of the neural phenotype with the mutant protein altering MT function, resulting in semidominant "poisoning" of the MTs. This leads to GCN dysfunction and cell death. In *Tubb4a*$^{Jit/+}$ heterozygotes, mutant *Tubb4a*^{Jit} protein would be expected to be 30% of the total b-tubulin, half of the amount of homozygous mutants (60%). *Tubb4a*$^{Jit/null}$ mutants, which, similar to *Tubb4a*$^{Jit/+}$ heterozygotes, harbor a single allele of the missense, have much stronger phenotype correlating with the larger percentage (~50%) of mutant protein relative to total β-tubulin. *Tubb4a*$^{Jit/Jit}$ mutants have the strongest phenotype with predicted ~60% of the β-tubulin harboring the missense. *Tubb4a* deletion does not result in a detectable phenotype. Mild phenotype: *Tubb4a*$^{Jit/+}$ mice have normal life span with slow degeneration of myelin and GCNs. Strong phenotype: *Tubb4a*$^{Jit/null}$ shows strong hypomyelination and almost complete GCN degeneration with death by ~3 months. Very strong phenotype: *Tubb4a*$^{Jit/Jit}$, the most severe hypomyelination and near-complete GCN degeneration by P48.

modifications. Tubulin mutations could potentially lead to pathology by generating MTs with an imbalanced tubulin isotype composition that could change the tubulin code or could cause a deficiency in available tubulin required to build an effective MT cytoskeleton.

We found that the phenotypes in *Jit* were not due to disruption of the code established by the balance of tubulin isotype proteins, as *Tubb4a* deletion did not cause a phenotype in the mouse, but rather the result of the expression of a dominant-acting mutant tubulin. Although the majority of β-tubulin transcription in GCNs and oligodendrocytes derived from *Tubb4a*, these cells were able to compensate for the loss of *Tubb4a* by the up-regulated expression of other β-tubulin family members. Not surprisingly, given the importance of tubulins and MTs for all cells, the total level of tubulin transcription appeared tightly controlled as deletion of *Tubb4a* did not affect the total levels of β-tubulin transcription. This result is consistent with reports that showed that total tubulin levels remained unchanged in tubulin isotype gene knockouts in the mouse: Total tubulin mRNA did not change in the tissues of the *Tubb3* knockout (38), and neither knockouts *Tubb2a* nor *Tubb2b* changed the total amount of tubulin protein compared with controls (39). These observations indicate that β-tubulins can function interchangeably depending on the isotype and the cellular context. We found that the different cell types compensated for loss of *Tubb4a* using different strategies. GCNs compensated for the loss of *Tubb4a* primarily by the strong transcriptional up-regulation of a single β-tubulin isotype gene *Tubb2a*, while oligodendrocytes relied on the modest transcriptional up-regulation of several of β-tubulin isotype genes. The ability of cell types to successfully compensate for the loss a tubulin gene may therefore depend on their ability to up-regulate other tubulin members.

Tubulinopathies are dominant disorders; however, the genetic basis of the pathologies is not well understood. Our analysis of an allelic series of *Tubb4a* in mice showed that the *Jit* mutation caused pathology through dominant negative activity and not because of loss of gene function. The antimorphic activity of the *Jit* mutation did not act to disrupt WT *Tubb4a* gene function, which is redundant and dispensable in the mouse, but rather acts as dominant negative for MT function likely by affecting kinesin interactions. The MT composition of tubulin isotypes is dependent on the intracellular concentrations of α- and β-tubulins, which incorporate freely into the MT polymer in a 1:1 stoichiometric ratio (50). We show that the strength of neural phenotypes in *Jit* mice correlated with its expression ratio compared with β-tubulins in tissues affected. GCNs and oligodendrocytes were strongly affected by *Jit*, resulting in apoptosis due to the high expression ratio of *Tubb4a*. Tissues with low expression ratios of *Tubb4a* did not have overt phenotypes in the mouse, likely because the dominant-acting *Tubb4a*^{Jit} was below threshold to strongly affect MTs. However, it is probable that mutant *Jit* protein affects MTs to some degree in all tissues where it is expressed. Nearly all cases of human tubulinopathies are associated with de novo heterozygous amino acid substitutions and not null mutations. On the basis of our analysis of *Jit*, we propose that the tissue specificity and degree of pathology in most tubulinopathies are determined by the expression ratio of a mutant tubulin in relation to the other tubulin family members in its class (α or β), which would vary from cell type to cell type in the body, as well as the strength of the specific dominant-acting missense. Specialized cells such as neurons are likely more susceptible to MT perturbations, which would account for the multitude of tubulinopathies affecting

the CNS. Tissues that express a more balanced tubulin isotype repertoire, without a strong expression ratio of a single tubulin isotype, would be predicted to be less susceptible to pathology because of dominant-acting tubulin mutations. In this model, therapeutic strategies that act to down-regulate the mutant tubulin expression or to dilute the mutant tubulin representation in MTs by increasing the expression of WT tubulin isotypes of the same class (β in the case of *Tubb4a*-related diseases) could potentially ameliorate cellular pathology and the disease course in tubulinopathies.

Tubulins and neural degeneration

Leukodystrophies comprise a diverse group of genetic diseases that lead to the abnormal development or destruction of the myelin sheath. Oligodendrocytes function to generate myelin and are essential support cells for neurons. Determining the degree to which neuronal phenotypes in leukodystrophies is due to cell-autonomous effects of the mutant gene in neurons or secondary to lack of supportive myelin is challenging. Several leukodystrophies are associated with cerebellar neuronal phenotypes in addition to H-ABC, leading to the hypothesis that hypomyelination plays a role in GCN degeneration (*21*). In this study, we have used conditional genetics in the mouse to test the role of myelination in GCN homeostasis and found that neurodegeneration is largely due to cell-autonomous effects of the *Tubb4a^Jit^* mutation within the GCN lineage and is largely independent of the levels of myelination. Disruption of MT function in GCN could result in defects in the transport of essential cargos, delivery of mitochondria, and the disruption of lysosomal function, among other essential MT-dependent cellular processes (*57*).

MTs play a crucial role in neurodevelopment, and mutations in tubulin isotype genes most commonly result in cerebral cortical patterning defects through the disruption of cell proliferation, neuronal migration, and other developmental pathways (*1*). In contrast, the *Jit* mutation did not appear to affect the development, migration, and differentiation of neurons but rather caused the degeneration of GCNs that were fully differentiated and that have completed their migration. We did not detect *Tubb4a* expression in GCN precursors that populate the external granule cell layer of the cerebellum where proliferation occurs. The IGL was similar in size to WT in *Tubb4a^Jit/Jit^* mutants at P21, indicating the proper generation and migration of GCNs, and DiI labeling showed that the neurons appeared mature with their characteristic morphology of four to five clawed dendrites. We only observed *Tubb4a* expression commencing in the IGL where GCNs reside after their migration and differentiation. The expression of the *Jit* mutation within differentiated GCNs caused notable degeneration by apoptosis of the most numerous neurons in the brain within a few weeks in *Tubb4a^Jit/Jit^* mutants, and more gradual cell death over a prolonged time course in *Tubb4a^Jit/+^* mutants. The cause of neuronal death in many human neurodegenerative diseases is a subject of intense current research and remains poorly understood. However, dysfunction of MTs and MT transport is hypothesized to be a critical common process leading to neuronal death in the diseases (*58*–*60*). Here, we provide an example that a primary tubulin mutation whose expression is initiated postdevelopmentally in a differentiated neuron is sufficient to cause cell death by apoptosis in a dosage-dependent manner in vivo in the mouse. These observations are consistent with a causative association of MT dysfunction with neurodegenerative disease (*58*–*60*). These studies highlight the critical importance of MT function for the survival and maintenance of neurons.

MATERIALS AND METHODS
Mouse strains
A three-generation screen for recessive ENU-induced mutations was performed by mutagenizing C57BL6 (Jackson Laboratory) male mice and outcrossing to FVB/NJ females (*41*). The *Jit* mutation was identified by a tremulous phenotype that was evident as early as P10 in N3 pups that were potentially homozygous for induced mutations. The *Jit* mutation was mapped to a segment of chromosome 17 based on the identification of regions homozygous for C57BL6/J polymorphisms in DNA from phenotypic mice on a genome-wide SNP panel (*61*). Subsequent genetic mapping of meiotic recombinants based on linkage to SNP and SSLPs on B6 chromosomes narrowed the interval to ~185-kb region between SNP markers rs33574324 and rs33478508 (Ensemble build GRCm38), which contained 10 genes. A T1242A transition was found in the gene *Tubb4a*, which is predicted to create an N414K missense in the Tubb4a protein. The *Jit* mutation was analyzed on the FVB background (>10 generations). Mice harboring a targeted knockout allele of *Tubb4a^tm1(KOMP)Wtsi^* (referred to as *Tubb4a^null^*) were generated from embryonic stem (ES) cells obtained from the International Knockout Mouse Consortium and were analyzed on the FVB background. Mice harboring a floxed allele of *Tubb4a* (referred to as *Tubb4a^fl^*) were generated from a cross between mice generated from ES cells procured from European conditional mouse mutagenesis program (EUCOMM) (Helmholz Zentrum, Muenchen), *Tubb4a^tm1a(EUCOMM)^*, and *actin-flp* mice (Jackson Laboratory, 005703). Mouse strains *Atoh1-cre* [B6.Cg-Tg (Atoh1-cre)1Bfri/J; JAX, stock #011104 (*49*)] and NG2-cre [B6;FVB-*Ifi208^Tg(Cspg4-cre)1Akik^*/J; JAX, stock #008533 (*48*)] have been previously described. See fig. S4 for maps of the *Tubb4a* targeted alleles. Mice containing conditional deletions of *Tubb4a* using cre/lox were analyzed on an FVB mixed background. All animal studies were performed under an approved Institutional Animals Care and Use Committee mouse protocol according to Yale University institutional guidelines.

Histology
Mice were perfused with cold 4% paraformaldehyde (PFA), and the CNS was dissected and immersion postfixed overnight (O/N) in 4% PFA at 4°C. CNS were transferred in 30% sucrose O/N and frozen in OCT compound (optimum cutting temperature) (Tissue-Tek). Cryosectioning was performed at 40 μm.

Eri-C staining
Slides were postfixed for 1 hour in 4% PFA, rinsed in phosphate-buffered saline (PBS), acetone treated for 5 min, rinsed in PBS, and immersed in Eri-C solution [0.2% eriochrome cyanine R (Millipore Sigma, 1031640025), 0.5% sulfuric acid (JT Baker, 9681-00), and 0.4% ferric ammonium sulfate (Thermo Fisher Scientific, I75-500)] for 30 min. Sections were differentiated in 5% ferric ammonium sulfate for 1 to 10 min, followed by a second differentiation in borax-ferricyanide solution [0.03 M sodium tetraborate (Thermo Fisher Scientific, S246-500) and 0.04 M potassium ferricyanide (Thermo Fisher Scientific, P232-500)] for 2 to 5 min.

Nissl (cresyl violet) staining
Slides were initially rinsed in PBS, immersed in cresyl violet solution [0.1% cresyl violet (Acros Organics, 229630050) and 0.1% acetic acid (JT Baker, 9508-00)] for 30 min, dipped in water, and differentiated in 70% ethanol, 1% acetic acid for 10 s. After staining, slides were dehydrated in ethanol and mounted in Cytoseal (Thermo Fisher Scientific, 8310-4).

Quantification of intensity of Eri-C staining and IGL surface area

Eri-C staining intensity was assessed on coronal sections of the forebrain and midline sagittal section of the hindbrain using ImageJ. Images of Eri-C staining were converted to grayscale images; samples from the CC and anterior commissures were used and averaged to assess the staining intensity in the forebrain and samples from the cerebellar white matter, brainstem, and dorsal and ventral anterior spinal cord to assess the intensity in the hindbrain. Within each section, a baseline intensity was determined based on of the intensity of staining in a region that is not myelinated (layer 1 of the neocortex for the forebrain, and the ML of the cerebellar for the hindbrain). The baseline intensity was subtracted from the intensity measured in the myelinated regions. Midline sagittal sections from the cerebellum stained for Nissl were used to measure the IGL surface area in ImageJ. The IGL was outlined, and its surface area was measured. Measurements from three animals of each genotype were averaged for comparisons.

Immunohistochemistry

For immunohistochemistry using 3,3′-Diaminobenzidine (DAB) detection, slides were incubated in 1% hydrogen peroxide for 30 min before blocking. Sections were blocked in 10% normal goat serum, 0.3% Triton X-100, and PBS for 1 hour at room temperature. Primary antibodies: Rabbit anti-cleaved Casp3 (1:600; Cell Signaling Technology, 9661) and rabbit anti-calbindin (1:10,000; Swant, CB-38a) were incubated O/N at 4°C in blocking solution. After washing in PBS, tissue was incubated with a secondary antibody [goat biotinylated anti-rabbit (Vector Laboratories, BA-1000)] 1:500 dilution in PBS for 2 hours at room temperature. Sections were washed in PBS and incubated for 1 hour in ABC solution (Vector Laboratories, PK-6100). Color reaction was performed using a DAB kit (Vector Laboratories, SK-4100). Sections were rinsed in PBS and dehydrated in increasing gradient of ethanol solutions (2 to 3 min each) and xylenes (3 min). After dehydration, sections were mounted with Cytoseal (Thermo Fisher Scientific, 8310-4). Sections were imaged on a Zeiss Axioskop microscope (451485 El-einsatz) using a SpotFlex camera driven by Spot software (Spot Imaging Solutions version 4.6.1.41).

Quantification of cleaved caspase-3–positive cells

Positive cleaved caspase-3 cells in lobule III and lobule VII were counted in each cerebellar layer (ML, Purkinje cell layer, IGL, and white matter) on three 40-μm-thick sections (±500 μm around the midline). The surface area of each layer was measured using ImageJ. The average volumetric density was calculated for each lobule and each layer. $n = 3$ $Tubb4a^{Jit/Jit}$ and $n = 3$ WT animals were analyzed.

Assessment of motor function

Mice were acclimated to the room where the test was performed for at least 15 min. At the end of each session, mice were weighed. Grip strength: Grip strength was assessed before rotarod testing using a TSE grip strength meter (TSE). Each mouse was given five trials with 5-min rest between each trial, and the maximum strength (arbitrary units) normalized to mouse weight was reported. Rotarod: Mice were tested on an accelerating rotarod (0 to 40 rpm over 300 s) (Accumeter). They underwent three training sessions over three consecutive days and were tested on the fourth day (62). During each session, the mice went through four trials, with 15-min rest between each trial. The average latency to fall for each mouse on testing day was reported.

In situ hybridization

In situ hybridization was performed using an antisense riboprobe to $Tubb4a$ nucleotides 1523-2125 of the cDNA (comprising 3′ untranslated and part of the 3′ coding regions). Tissues were counterstained with Nuclear Fast Red. In situs on sections of the $Tubb4a^{null/null}$ CNS were used as negative controls. Images were taken on a Zeiss Axioscope microscope (451485 El-einsatz) using a SpotFlex camera driven by Spot software (Spot Imaging Solutions version 4.6.1.41).

Transmission electron microscopy

Mouse brain tissues were perfused in 4% PFA, sectioned at 100 μm on a vibratome, fixed in 2% glutaraldehyde, 2% PFA in 0.1 M sodium cacodylate buffer (pH 7.4) at room temperature for 1 hour, and postfixed in 1% OsO_4, 0.8% $K3Fe(CN)_6$ at room temperature for 1 hour. Specimens were stained en bloc with 2% aqueous uranyl acetate for 30 min, dehydrated in a graded series of ethanol to 100%, and embedded in Poly/Bed 812 resin. Blocks were polymerized in a 60°C oven overnight. Thin sections (60 nm) were cut by a Leica ultramicrotome and poststained with 2% uranyl acetate and lead citrate. Samples were examined with an FEI Tecnai transmission electron microscope at 80-kV accelerating voltage; digital images were recorded with an Olympus Morada charge-coupled device camera and iTEM imaging software.

PCR analyses

CNS regions of interest were microdissected in PBS using a tungsten needle and extracted in RNAeasy lysis buffer (RLT) lysis buffer (QIAGEN). Extraction of total RNA was performed using the RNeasy Plus Mini Kit (QIAGEN) according to the manufacturer's instructions. Reverse transcription was performed using the qScript cDNA SuperMix (QuantaBio) for PerfeCTa SYBR Green FastMix; ROX (QuantaBio) was used for qPCR. Amplification of β-tubulin transcripts was performed by using β-tubulin isotype-specific primers described in (7). A minimum of three biological and technical replicates were used per experiment. Verification of the recombined floxed allele used a three-primer PCR strategy with the following primers: GGGCTTTGGGGAGACACTGAC (recombined forward), GGGCTTTG-GGAGACACTGAC (nonrecombined forward), and TATATA-GAGAGTTGGTGGTT (reverse).

Expression of HA-tagged Tubb4a

C-terminal HA-tagged WT or $Tubb4a^{Jit}$ cDNA was cloned into the pcDNA 3.1 vector and transfected into retinal pigmented epithelial cell (RPE). RPE cells (1×10^5) were seeded onto coverslips in a 24-well plate. Two micrograms of plasmid DNA was used to transfect cells (Lipofectamine 3000, Thermo Fisher Scientific) following the manufacturer's instructions. Cells were fixed for 15 min with methanol 48 hours posttransfection and blocked with PBS with 0.1% Triton X-100 and 1% normal goat serum for 1 hour. The cells were incubated with the primary antibodies [rabbit anti–α-tubulin (Abcam) and rat anti-HA (Sigma-Aldrich)] overnight at 4°C, rinsed, and incubated with secondary antibodies [Alexa Fluor 488 donkey anti-rabbit (Life Technologies) and Alexa Fluor 594 goat anti-rat antibodies (Life Technologies)] for 1 hour at room temperature. Images were obtained on a Zeiss Axiovert microscope using a Hamamatsu Oraca Flash 4.0 camera driven by Zen software.

DiI tracing

After perfusion with 4% PFA, the cerebellum was dissected and postfixed by immersion in 4% PFA at least overnight. Crystals of DiI (D3911, Invitrogen) were inserted on the surface of the cerebellum in the ML to target the axons of the GCNs so their cell bodies could be retrogradely labeled. Crystals were kept in place with 6% agarose. The cerebellums were then placed in 4% PFA at 37°C for 3 to 7 days. Cerebellums were sectioned (30 μm) using a vibratome (Leica VT1200S) and placed onto slides to adhere before mounting with Mowiol. Images were obtained on a Zeiss Axioskop microscope (451485 El-einsatz) using a SpotFlex camera driven by Spot software (Spot Imaging Solutions version 4.6.1.41).

Statistics

Statistical analysis was performed with the GraphPad Prism 7 software package. For comparison of number of CASP3-positive cells and the total amount of β-tubulin between *Tubb4a* alleles, we performed one-way analysis of variance (ANOVA) with Tukey's multiple comparisons test. For comparison of the expression levels of each β-tubulin isotype between *Tubb4a* alleles and rotarod tests, we performed two-way ANOVA with Tukey's multiple comparisons test. Significance was achieved for $P < 0.05$.

SUPPLEMENTARY MATERIALS

Supplementary material for this article is available at https://science.org/doi/10.1126/sciadv.abf7262

View/request a protocol for this paper from *Bio-protocol*.

REFERENCES AND NOTES

1. M. W. Breuss, I. Leca, T. Gstrein, A. H. Hansen, D. A. Keays, Tubulins and brain development—The origins of functional specification. *Mol. Cell. Neurosci.* **84**, 58–67 (2017).
2. M. Breuss, D. A. Keays, Microtubules and neurodevelopmental disease: The movers and the makers, in *Cellular and Molecular Control of Neuronal Migration*, L. Nguyen, S. Hippenmeyer, Eds. (Springer Netherlands, 2014), pp. 75–96.
3. D. A. Keays, Neuronal migration: Unraveling the molecular pathway with humans, mice, and a fungus. *Mamm. Genome* **18**, 425–430 (2007).
4. A. Okumura, M. Hayashi, H. Tsurui, Y. Yamakawa, S. Abe, T. Kudo, R. Suzuki, T. Shimizu, K. Shimojima, T. Yamamoto, Lissencephaly with marked ventricular dilation, agenesis of corpus callosum, and cerebellar hypoplasia caused by TUBA1A mutation. *Brain Dev.* **35**, 274–279 (2013).
5. X. H. Jaglin, K. Poirier, Y. Saillour, E. Buhler, G. Tian, N. Bahi-Buisson, C. Fallet-Bianco, F. Phan-Dinh-Tuy, X. P. Kong, P. Bomont, L. Castelnau-Ptakhine, S. Odent, P. Loget, M. Kossorotoff, I. Snoeck, G. Plessis, P. Parent, C. Beldjord, C. Cardoso, A. Represa, J. Flint, D. A. Keays, N. J. Cowan, J. Chelly, Mutations in the beta-tubulin gene TUBB2B result in asymmetrical polymicrogyria. *Nat. Genet.* **41**, 746–752 (2009).
6. C. Fallet-Bianco, L. Loeuillet, K. Poirier, P. Loget, F. Chapon, L. Pasquier, Y. Saillour, C. Beldjord, J. Chelly, F. Francis, Neuropathological phenotype of a distinct form of lissencephaly associated with mutations in TUBA1A. *Brain* **131**, 2304–2320 (2008).
7. M. Breuss, J. I. Heng, K. Poirier, G. Tian, X. H. Jaglin, Z. Qu, A. Braun, T. Gstrein, L. Ngo, M. Haas, N. Bahi-Buisson, M. L. Moutard, S. Passemard, A. Verloes, P. Gressens, Y. Xie, K. J. Robson, D. S. Rani, K. Thangaraj, T. Clausen, J. Chelly, N. J. Cowan, D. A. Keays, Mutations in the β-tubulin gene TUBB5 cause microcephaly with structural brain abnormalities. *Cell Rep.* **2**, 1554–1562 (2012).
8. N. Bahi-Buisson, K. Poirier, N. Boddaert, Y. Saillour, N. Castelnau, N. Philip, G. Buyse, L. Villard, S. Joriot, S. Marret, M. Bourgeois, H. Van Esch, L. Lagae, J. Amiel, L. Hertz-Pannier, A. Roubertie, F. Rivier, J. M. Pinard, C. Beldjord, J. Chelly, Refinement of cortical dysgeneses spectrum associated with TUBA1A mutations. *J. Med. Genet.* **45**, 647–653 (2008).
9. K. Poirier, Y. Saillour, N. Bahi-Buisson, X. H. Jaglin, C. Fallet-Bianco, R. Nabbout, L. Castelnau-Ptakhine, A. Roubertie, T. Attie-Bitach, I. Desguerre, D. Genevieve, C. Barnerias, B. Keren, N. Lebrun, N. Boddaert, F. Encha-Razavi, J. Chelly, Mutations in the neuronal ss-tubulin subunit TUBB3 result in malformation of cortical development and neuronal migration defects. *Hum. Mol. Genet.* **19**, 4462–4473 (2010).
10. G. Y. Cederquist, A. Luchniak, M. A. Tischfield, M. Peeva, Y. Song, M. P. Menezes, W. M. Chan, C. Andrews, S. Chew, R. V. Jamieson, L. Gomes, M. Flaherty, P. E. Grant, M. L. Gupta Jr., E. C. Engle, An inherited TUBB2B mutation alters a kinesin-binding site and causes polymicrogyria, CFEOM and axon dysinnervation. *Hum. Mol. Genet.* **21**, 5484–5499 (2012).
11. C. Fallet-Bianco, A. Laquerriere, K. Poirier, F. Razavi, F. Guimiot, P. Dias, L. Loeuillet, K. Lascelles, C. Beldjord, N. Carion, A. Toussaint, N. Revencu, M. C. Addor, B. Lhermitte, M. Gonzales, J. Martinovich, B. Bessieres, M. Marcy-Bonniere, F. Jossic, P. Marcorelles, P. Loget, J. Chelly, N. Bahi-Buisson, Mutations in tubulin genes are frequent causes of various foetal malformations of cortical development including microlissencephaly. *Acta Neuropathol. Commun.* **2**, 69 (2014).
12. M. A. Tischfield, H. N. Baris, C. Wu, G. Rudolph, L. Van Maldergem, W. He, W. M. Chan, C. Andrews, J. L. Demer, R. L. Robertson, D. A. Mackey, J. B. Ruddle, T. D. Bird, I. Gottlob, C. Pieh, E. I. Traboulsi, S. L. Pomeroy, D. G. Hunter, J. S. Soul, A. Newlin, L. J. Sabol, E. J. Doherty, C. E. de Uzcategui, N. de Uzcategui, M. L. Collins, E. C. Sener, B. Wabbels, H. Hellebrand, T. Meitinger, T. de Berardinis, A. Magli, C. Schiavi, M. Pastore-Trossello, F. Koc, A. M. Wong, A. V. Levin, M. T. Geraghty, M. Descartes, M. Flaherty, R. V. Jamieson, H. U. Moller, I. Meuthen, D. F. Callen, J. Kerwin, S. Lindsay, A. Meindl, M. L. Gupta Jr., D. Pellman, E. C. Engle, Human TUBB3 mutations perturb microtubule dynamics, kinesin interactions, and axon guidance. *Cell* **140**, 74–87 (2010).
13. M. A. Tischfield, G. Y. Cederquist, M. L. Gupta Jr., E. C. Engle, Phenotypic spectrum of the tubulin-related disorders and functional implications of disease-causing mutations. *Curr. Opin. Genet. Dev.* **21**, 286–294 (2011).
14. R. Luscan, S. Mechaussier, A. Paul, G. Tian, X. Gerard, S. Defoort-Dellhemmes, N. Loundon, I. Audo, S. Bonnin, J. F. LeGargasson, J. Dumont, N. Goudin, M. Garfa-Traore, M. Bras, A. Pouliet, B. Bessieres, N. Boddaert, J. A. Sahel, S. Lyonnet, J. Kaplan, N. J. Cowan, J. M. Rozet, S. Marlin, I. Perrault, Mutations in TUBB4B cause a distinctive sensorineural disease. *Am. J. Hum. Genet.* **101**, 1006–1012 (2017).
15. V. Pensato, C. Tiloca, L. Corrado, C. Bertolin, V. Sardone, R. Del Bo, D. Calini, J. Mandrioli, G. Lauria, L. Mazzini, G. Querin, M. Ceroni, R. Cantello, S. Corti, B. Castellotti, G. Solda, S. Duga, G. P. Comi, C. Cereda, G. Soraru, S. D'Alfonso, F. Taroni, C. E. Shaw, J. E. Landers, N. Ticozzi, A. Ratti, C. Gellera, V. Silani; SLAGEN Consortium, TUBA4A gene analysis in sporadic amyotrophic lateral sclerosis: Identification of novel mutations. *J. Neurol.* **262**, 1376–1378 (2015).
16. B. N. Smith, N. Ticozzi, C. Fallini, A. S. Gkazi, S. Topp, K. P. Kenna, E. L. Scotter, J. Kost, P. Keagle, J. W. Miller, D. Calini, C. Vance, E. W. Danielson, C. Troakes, C. Tiloca, S. Al-Sarraj, E. A. Lewis, A. King, C. Colombrita, V. Pensato, B. Castellotti, J. de Belleroche, F. Baas, A. L. Ten Asbroek, P. C. Sapp, D. McKenna-Yasek, R. L. McLaughlin, M. Polak, S. Asress, J. Esteban-Perez, J. L. Munoz-Blanco, M. Simpson, W. van Rheenen, F. P. Diekstra, G. Lauria, S. Duga, S. Corti, C. Cereda, L. Corrado, G. Soraru, K. E. Morrison, K. L. Williams, G. A. Nicholson, I. P. Blair, P. A. Dion, C. S. Leblond, G. A. Rouleau, O. Hardiman, J. H. Veldink, L. H. van den Berg, A. Al-Chalabi, H. Pall, P. J. Shaw, M. R. Turner, K. Talbot, F. Taroni, A. Garcia-Redondo, Z. Wu, J. D. Glass, C. Gellera, A. Ratti, R. H. Brown Jr., V. Silani, C. E. Shaw, J. E. Landers, Exome-wide rare variant analysis identifies TUBA4A mutations associated with familial ALS. *Neuron* **84**, 324–331 (2014).
17. H. D. Schwer, P. Lecine, S. Tiwari, J. E. Italiano Jr., J. H. Hartwig, R. A. Shivdasani, A lineage-restricted and divergent beta-tubulin isoform is essential for the biogenesis, structure and function of blood platelets. *Curr. Biol.* **11**, 579–586 (2001).
18. R. Feng, Q. Sang, Y. Kuang, X. Sun, Z. Yan, S. Zhang, J. Shi, G. Tian, A. Luchniak, Y. Fukuda, B. Li, M. Yu, J. Chen, Y. Xu, L. Guo, R. Qu, X. Wang, Z. Sun, M. Liu, H. Shi, H. Wang, Y. Feng, R. Shao, R. Chai, Q. Li, R. Xing, R. Zhang, E. Nogales, L. Jin, L. He, M. L. Gupta Jr., N. J. Cowan, L. Wang, Mutations in TUBB8 and human oocyte meiotic arrest. *N. Engl. J. Med.* **374**, 223–232 (2016).
19. C. Simons, N. I. Wolf, N. McNeil, L. Caldovic, J. M. Devaney, J. Takanohashi, J. Crawford, K. Ru, S. M. Grimmond, D. Miller, D. Tonduti, J. L. Schmidt, R. S. Chudnow, R. van Coster, L. Lagae, J. Kisler, J. Sperner, M. S. van der Knaap, R. Schiffmann, R. J. Taft, A. Vanderver, A de novo mutation in the β-tubulin gene TUBB4A results in the leukoencephalopathy hypomyelination with atrophy of the basal ganglia and cerebellum. *Am. J. Hum. Genet.* **92**, 767–773 (2013).
20. I. D. Duncan, M. Bugiani, A. B. Radcliff, J. J. Moran, C. Lopez-Anido, P. Duong, B. K. August, N. I. Wolf, M. S. van der Knaap, J. Svaren, A mutation in the Tubb4a gene leads to microtubule accumulation with hypomyelination and demyelination. *Ann. Neurol.* **81**, 690–702 (2017).
21. J. Curiel, G. Rodriguez Bey, A. Takanohashi, M. Bugiani, X. Fu, N. I. Wolf, B. Nmezi, R. Schiffmann, M. Bugaighis, T. Pierson, G. Helman, C. Simons, M. S. van der Knaap, J. Liu, Q. Padiath, A. Vanderver, TUBB4A mutations result in specific neuronal and oligodendrocytic defects that closely match clinically distinct phenotypes. *Hum. Mol. Genet.* **26**, 4506–4518 (2017).
22. K. Lohmann, R. A. Wilcox, S. Winkler, A. Ramirez, A. Rakovic, J. S. Park, B. Arns, T. Lohnau, J. Groen, M. Kasten, N. Bruggemann, J. Hagenah, A. Schmidt, F. J. Kaiser, K. R. Kumar, K. Zschiedrich, D. Alvarez-Fischer, E. Altenmuller, A. Ferbert, A. E. Lang, A. Munchau, V. Kostic, K. Simonyan, M. Agzarian, I. J. Ozelius, A. P. Langeveld, C. M. Sue, M. A. Tijssen, C. Klein, Whispering dysphonia (DYT4 dystonia) is caused by a mutation in the TUBB4 gene. *Ann. Neurol.* **73**, 537–545 (2013).

23. J. Hersheson, N. E. Mencacci, M. Davis, N. Macdonald, D. Trabzuni, M. Ryten, A. Pittman, R. Paudel, E. Kara, K. Fawcett, V. Plagnol, K. P. Bhatia, A. J. Medlar, H. C. Stanescu, J. Hardy, R. Kleta, N. W. Wood, H. Houlden, Mutations in the autoregulatory domain of β-tubulin 4a cause hereditary dystonia. *Ann. Neurol.* **73**, 546–553 (2013).

24. A. Pizzino, T. M. Pierson, Y. Guo, G. Helman, S. Fortini, K. Guerrero, S. Saitta, J. L. Murphy, Q. Padiath, Y. Xie, H. Hakonarson, X. Xu, T. Funari, M. Fox, R. J. Taft, M. S. van der Knaap, G. Bernard, R. Schiffmann, C. Simons, A. Vanderver, TUBB4A de novo mutations cause isolated hypomyelination. *Neurology* **83**, 898–902 (2014).

25. M. Sirajuddin, L. M. Rice, R. D. Vale, Regulation of microtubule motors by tubulin isotypes and post-translational modifications. *Nat. Cell Biol.* **16**, 335–344 (2014).

26. C. Janke, M. M. Magiera, The tubulin code and its role in controlling microtubule properties and functions. *Nat. Rev. Mol. Cell Biol.* **21**, 307–326 (2020).

27. S. Chakraborti, K. Natarajan, J. Curiel, C. Janke, J. Liu, The emerging role of the tubulin code: From the tubulin molecule to neuronal function and disease. *Cytoskeleton* **73**, 521–550 (2016).

28. R. F. Luduena, Multiple forms of tubulin: Different gene products and covalent modifications. *Int. Rev. Cytol.* **178**, 207–275 (1998).

29. E. C. Raff, J. D. Fackenthal, J. A. Hutchens, H. D. Hoyle, F. R. Turner, Microtubule architecture specified by a β-tubulin isoform. *Science* **275**, 70–73 (1997).

30. C. Savage, M. Hamelin, J. G. Culotti, A. Coulson, D. G. Albertson, M. Chalfie, mec-7 is a beta-tubulin gene required for the production of 15-protofilament microtubules in *Caenorhabditis elegans*. *Genes Dev.* **3**, 870–881 (1989).

31. S. C. Ti, G. M. Alushin, T. M. Kapoor, Human β-tubulin isotypes can regulate microtubule protofilament number and stability. *Dev. Cell* **47**, 175–190.e5 (2018).

32. L. J. Leandro-Garcia, S. Leskela, I. Landa, C. Montero-Conde, E. Lopez-Jimenez, R. Leton, A. Cascon, M. Robledo, C. Rodriguez-Antona, Tumoral and tissue-specific expression of the major human beta-tubulin isotypes. *Cytoskeleton* **67**, 214–223 (2010).

33. T. J. Hausrat, J. Radwitz, F. L. Lombino, P. Breiden, M. Kneussel, Alpha- and beta-tubulin isotypes are differentially expressed during brain development. *Dev. Neurobiol.* **81**, 333–350 (2021).

34. C. Janke, The tubulin code: Molecular components, readout mechanisms, and functions. *J. Cell Biol.* **206**, 461–472 (2014).

35. A. Roll-Mecak, The tubulin code in microtubule dynamics and information encoding. *Dev. Cell* **54**, 7–20 (2020).

36. C. Fulton, P. A. Simpson, Selective synthesis and utilization of flagellar tubulin: The multi-tubulin hypothesis, in *Cell motility* R. D. Goldman, T. Pollard, J. Rosenbaum, Eds. (Cold Spring Harbor conferences on cell proliferation, Cold Spring Harbor Laboratory, Cold Spring Harbor, N.Y., 1976)

37. M. Breuss, T. Fritz, K. Gstrein, L. Chan, L. Ushakova, N. Yu, F. W. Vonberg, B. Werner, U. Elling, D. A. Keays, Mutations in the murine homologue of TUBB5 cause microcephaly by perturbing cell cycle progression and inducing p53-associated apoptosis. *Development* **143**, 1126–1133 (2016).

38. A. Latremoliere, L. Cheng, M. DeLisle, C. Wu, S. Chew, E. B. Hutchinson, A. Sheridan, C. Alexandre, F. Latremoliere, S. H. Sheu, S. Golidy, T. Omura, E. A. Huebner, Y. Fan, M. C. Whitman, E. Nguyen, C. Hermawan, C. Pierpaoli, M. A. Tischfield, C. J. Woolf, E. C. Engle, Neuronal-specific TUBB3 is not required for normal neuronal function but is essential for timely axon regeneration. *Cell Rep.* **24**, 1865–1879.e9 (2018).

39. E. Bittermann, Z. Abdelhamed, R. P. Liegel, C. Menke, A. Timms, D. R. Beier, R. W. Stottmann, Differential requirements of tubulin genes in mammalian forebrain development. *PLOS Genet.* **15**, e1008243 (2019).

40. J. Aiken, G. Buscaglia, A. S. Aiken, J. K. Moore, E. A. Bates, Tubulin mutations in brain development disorders: Why haploinsufficiency does not explain *TUBA1A* tubulinopathies. *Cytoskeleton* **77**, 40–54 (2020).

41. K. F. Liem Jr., M. He, P. J. Ocbina, K. V. Anderson, Mouse Kif7/Costal2 is a cilia-associated protein that regulates Sonic hedgehog signaling. *Proc. Natl. Acad. Sci. U.S.A.* **106**, 13377–13382 (2009).

42. S. Sase, A. A. Almad, C. A. Boecker, P. Guedes-Dias, J. J. Li, A. Takanohashi, A. Patel, T. McCaffrey, H. Patel, D. Sirdeshpande, J. Curiel, J. Shih-Hwa Liu, Q. Padiath, E. L. Holzbaur, S. S. Scherer, A. Vanderver, *TUBB4A* mutations result in both glial and neuronal degeneration in an H-ABC leukodystrophy mouse model. *eLife* **9**, e52986 (2020).

43. H. L. Paulson, V. G. Shakkottai, H. B. Clark, H. T. Orr, Polyglutamine spinocerebellar ataxias—From genes to potential treatments. *Nat. Rev. Neurosci.* **18**, 613–626 (2017).

44. J. Altman, S. A. Bayer, *Development of the Cerebellar System: In Relation to its Evolution, Structure, and Functions* (CRC Press, 1997).

45. R. V. Sillitoe, A. L. Joyner, Morphology, molecular codes, and circuitry produce the three-dimensional complexity of the cerebellum. *Annu. Rev. Cell Dev. Biol.* **23**, 549–577 (2007).

46. A. Sudarov, A. L. Joyner, Cerebellum morphogenesis: The foliation pattern is orchestrated by multi-cellular anchoring centers. *Neural Dev.* **2**, 26 (2007).

47. F. Vulinovic, V. Krajka, T. J. Hausrat, P. Seibler, D. Alvarez-Fischer, H. Madoev, J. S. Park, K. R. Kumar, C. M. Sue, K. Lohmann, M. Kneussel, C. Klein, A. Rakovic, Motor protein binding and mitochondrial transport are altered by pathogenic TUBB4A variants. *Hum. Mutat.* **39**, 1901–1915 (2018).

48. X. Zhu, D. E. Bergles, A. Nishiyama, NG2 cells generate both oligodendrocytes and gray matter astrocytes. *Development* **135**, 145–157 (2008).

49. V. Matei, S. Pauley, S. Kaing, D. Rowitch, K. W. Beisel, K. Morris, F. Feng, K. Jones, J. Lee, B. Fritzsch, Smaller inner ear sensory epithelia in Neurog 1 null mice are related to earlier hair cell cycle exit. *Dev. Dyn.* **234**, 633–650 (2005).

50. S. A. Lewis, W. Gu, N. J. Cowan, Free intermingling of mammalian beta-tubulin isotypes among functionally distinct microtubules. *Cell* **49**, 539–548 (1987).

51. S. Uchimura, Y. Oguchi, M. Katsuki, T. Usui, H. Osada, J. Nikawa, S. Ishiwata, E. Muto, Identification of a strong binding site for kinesin on the microtubule using mutant analysis of tubulin. *EMBO J.* **25**, 5932–5941 (2006).

52. Y. Zhang, K. Chen, S. A. Sloan, M. L. Bennett, A. R. Scholze, S. O'Keeffe, H. P. Phatnani, P. Guarnieri, C. Caneda, N. Ruderisch, S. Deng, S. A. Liddelow, C. Zhang, R. Daneman, T. Maniatis, B. A. Barres, J. Q. Wu, An RNA-sequencing transcriptome and splicing database of glia, neurons, and vascular cells of the cerebral cortex. *J. Neurosci.* **34**, 11929–11947 (2014).

53. S. Fertuzinhos, M. Li, Y. I. Kawasawa, V. Ivic, D. Franjic, D. Singh, M. Crair, N. Sestan, Laminar and temporal expression dynamics of coding and noncoding RNAs in the mouse neocortex. *Cell Rep.* **6**, 938–950 (2014).

54. S. Niwa, H. Takahashi, N. Hirokawa, β-Tubulin mutations that cause severe neuropathies disrupt axonal transport. *EMBO J.* **32**, 1352–1364 (2013).

55. M. A. Tischfield, E. C. Engle, Distinct alpha- and beta-tubulin isotypes are required for the positioning, differentiation and survival of neurons: New support for the 'multi-tubulin' hypothesis. *Biosci. Rep.* **30**, 319–330 (2010).

56. S. C. Ti, M. C. Pamula, S. C. Howes, C. Duellberg, N. I. Cade, R. E. Kleiner, S. Forth, T. Surrey, E. Nogales, T. M. Kapoor, Mutations in human tubulin proximal to the kinesin-binding site alter dynamic instability at microtubule plus- and minus-ends. *Dev. Cell* **37**, 72–84 (2016).

57. E. Perlson, S. Maday, M. M. Fu, A. J. Moughamian, E. L. Holzbaur, Retrograde axonal transport: Pathways to cell death? *Trends Neurosci.* **33**, 335–344 (2010).

58. A. J. Matamoros, P. W. Baas, Microtubules in health and degenerative disease of the nervous system. *Brain Res. Bull.* **126**, 217–225 (2016).

59. S. T. Brady, G. A. Morfini, Regulation of motor proteins, axonal transport deficits and adult-onset neurodegenerative diseases. *Neurobiol. Dis.* **105**, 273–282 (2017).

60. J. Dubey, N. Ratnakaran, S. P. Koushika, Neurodegeneration and microtubule dynamics: Death by a thousand cuts. *Front. Cell. Neurosci.* **9**, 343 (2015).

61. J. L. Moran, A. D. Bolton, P. V. Tran, A. Brown, N. D. Dwyer, D. K. Manning, B. C. Bjork, C. Li, K. Montgomery, S. M. Siepka, M. H. Vitaterna, J. S. Takahashi, T. Wiltshire, D. J. Kwiatkowski, R. Kucherlapati, D. R. Beier, Utilization of a whole genome SNP panel for efficient genetic mapping in the mouse. *Genome Res.* **16**, 436–440 (2006).

62. R. J. Carter, J. Morton, S. B. Dunnett, Motor coordination and balance in rodents. *Curr. Protoc. Neurosci.* **Chapter 8**, Unit 8.12 (2001).